DEVELOPMENTAL BIOLOGY

Biogenesis of *C. elegans* spermatogenesis small RNAs is initiated by a zc3h12a-like ribonuclease

Hsin-Yue Tsai[1,2]*, Hsian-Tang Cheng[1], Yi-Ting Tsai[1]

Small RNAs regulate spermatogenesis across species ranging from *Caenorhabditis elegans* to humans. In *C. elegans*, two Argonaute proteins, ALG-3 and ALG-4, and their associated *alg-3/4* 26G-small RNAs are essential for spermiogenesis at 25°C. The *alg-3/4* 26G-small RNAs are antisense to their target mRNAs and produced by the RNA-dependent RNA polymerase, RRF-3. However, it remains unclear how the RNA templates for RRF-3 are generated and which cellular processes are affected by *alg-3/4* 26G-small RNAs. Here, we demonstrate a previously unidentified zc3h12a-like ribonuclease protein, NYN-3, in *alg-3/4* 26G-small RNAs biogenesis. NYN-3 is not only required for proper abundance of *alg-3/4* 26G-small RNAs but also crosslinked to their targeted mRNAs before RRF-3 from ePAR-CLIP-seq. Bioinformatics analysis was then used to parse the 26G-small RNA-targeted genes into functional subclasses. Collectively, these findings implicate NYN-3 as an initiator of *alg-3/4* 26G-small RNA generation.

INTRODUCTION

The molecular processes that control reproduction and fertility are often highly conserved. Small RNAs regulate male fertility and help to imprint paternally inherited epigenetic information. For example, spermiogenesis (the process of motile spermatozoa formation) is promoted by Piwi-interacting RNAs (piRNAs) in mice and *alg-3/4* 26G small RNAs in *Caenorhabditis elegans* (*1*–*3*).

The *alg-3/4* 26G small RNAs in *C. elegans* are 5′-monophosphorylated guanosine–containing 26-nt RNAs that are antisense to the mature mRNAs that they target (i.e., *alg-3/4*–targeted mRNAs). Furthermore, studies have shown that ALG-3 and ALG-4, two Argonaute family proteins with 96% amino acid identity, interact with *alg-3/4* 26G small RNAs to promote the recruitment of RNA polymerase II to genes essential for spermiogenesis at 25°C (*4*, *5*). The biogenesis of *alg-3/4* 26G small RNAs depends on RRF-3, which is part of the worm RNA-dependent RNA polymerase (RdRP) trio and a component of the ERI/DICER complex. In addition to RRF-3, more than 10 other proteins have been found to associate with RRF-3 during small RNA genesis. Moreover, studies that analyzed total sense RNAs related to *alg-3/4* 26G small RNAs uncovered a 22-nt sense RNA that is complementary to *alg-3/4* 26G small RNAs and contains 1- and 3-nt overhangs at the respective 5′ and 3′ termini of *alg-3/4* 26G small RNAs. While this observation suggests that the double-stranded RNA synthesized by RRF-3 is subject to DCR-1 processing, the mechanism underlying biogenesis of the initial RNA template is still unknown (*6*–*11*).

In mice, Zc3h12a-like NYN domain–containing ribonuclease is involved in targeted mRNA degradation, while in *C. elegans*, the Zc3h12a-like ribonuclease, RDE-8, was shown to promote small interfering RNA (siRNA) production by cleaving targeted mRNAs and generating [post-UG (Uridine and Guanosine) addition] RNA templates for siRNA synthesis by RRF-1 (*12*, *13*). C29F5.3 is the last uncharacterized Zc3h12a-like NYN domain–containing ribonuclease that contains all four aspartic acid residues to compose a catalytic tetrad. Here, we named this protein NYN-3 and sought to identify its function. Unexpectedly, our phenotypic characterization of *nyn-3* mutants as well as small RNA sequencing (RNA-seq) studies revealed that the level of *alg-3/4* 26G small RNAs depends on NYN-3. Moreover, we found that NYN-3 can bind and cleave in *alg-3/4*–targeted mRNAs. We also used the *nyn-3* mutants to inventory genes that are regulated by 5′- and 3′-targeted 26G small RNAs. Overall, our findings provide previously unidentified insights into the regulation of gene expression during spermatogenesis.

RESULTS

NYN-3 is essential for fertility at 25°C

NYN-3 is encoded by *c29f5.3* and comprises a ~42-kDa protein containing a zc3h12a-like ribonuclease NYN domain and a putative cytidine deaminase (CDA) domain (Fig. 1A and fig. S1A). To explore the function of NYN-3, we studied four different types of *nyn-3* mutants. First, we created *nyn-3 (ht044)*, a ribonuclease activity–defective mutant. In this strain, one of the conserved catalytic Asp residues in the zc3h12a-like ribonuclease NYN domain was mutated to Asn. The mutated site, Asp28, is equivalent to Asp141 in mouse Zc3h12a and Asp76 in RDE-8, which are both essential for the ribonuclease activity of the respective enzymes (*13*, *14*). Second, we used *nyn-3(tm2499)*, a deletion mutant lacking 68 amino acids in the putative CDA domain. Third, we generated a *nyn-3(ht056)* mutant in which only conserved residues in the *nyn-3* CDA domain were mutated (fig. S1A). The changes in this strain included mutating the Ala-Glu-Leu-Glu-Ala-Ile stretch to $(Ala)_6$ and altering the Gly downstream of Ala-Glu-Leu-Glu-Ala-Ile to Pro. Last, the *nyn-3(ht075)* is a null mutant in which part of second exon and the entire third exon are deleted, creating a frameshift and premature stop codon in the downstream amino acid sequence. Of note, there is no suitable antibody for NYN-3, so we used CRISPR-based genome editing to add a hemagglutinin (HA) tag to the N termini of wild-type (WT) *nyn-3* and the different *nyn-3* mutants.

Phenotypic characterizations of all four *nyn-3* mutants revealed marked effects on sterility at 25°C (Fig. 1B). The reductions in

[1]Institute of Molecular Medicine, College of Medicine, National Taiwan University, No. 7 Chung-Shan South Road, Taipei 10002, Taiwan. [2]Center of Precision Medicine, College of Medicine, National Taiwan University, No. 7 Chung-Shan South Road, Taipei 10002, Taiwan.
*Corresponding author. Email: hsinyuetsai@ntu.edu.tw

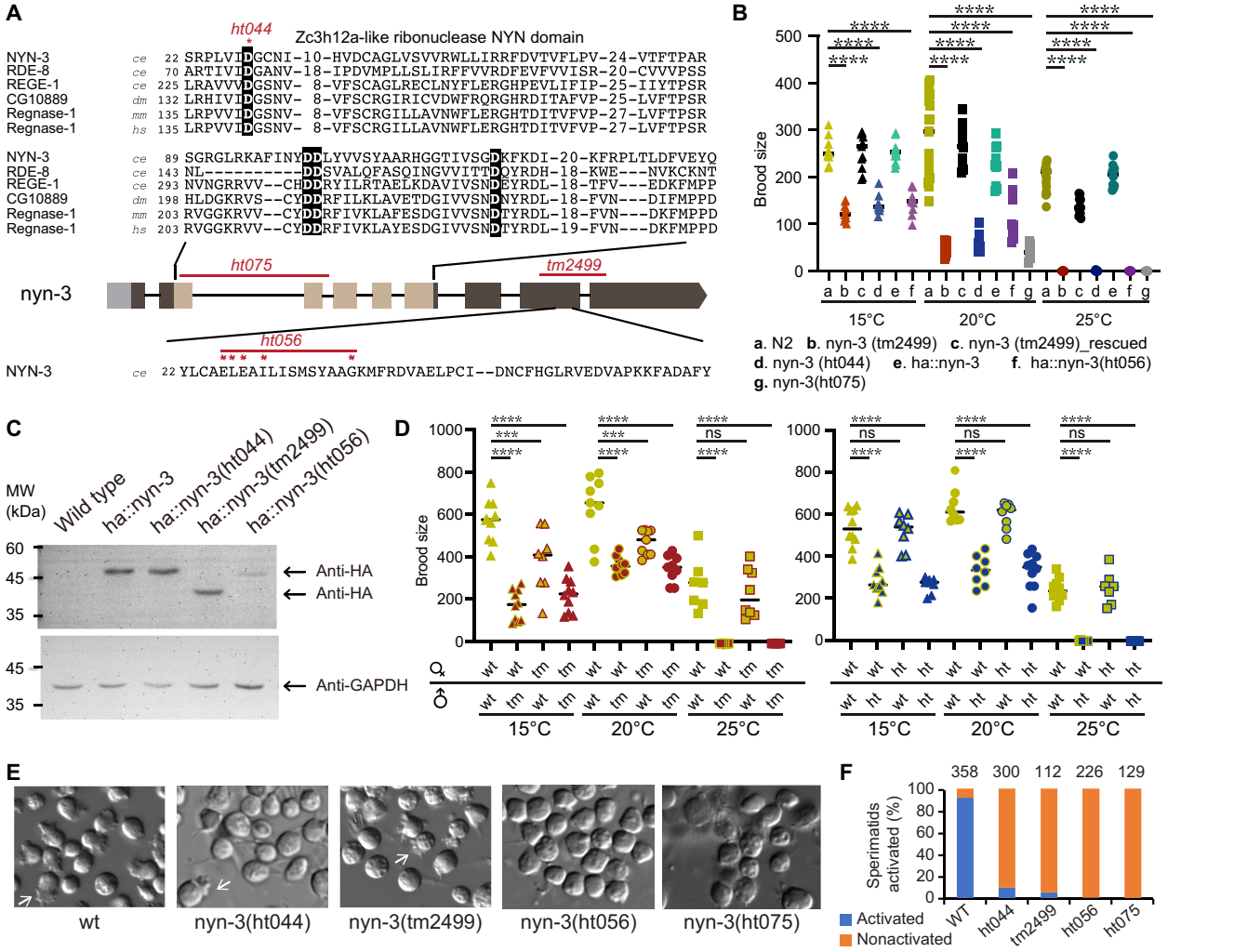

Fig. 1. NYN-3 ribonuclease domain is required for spermiogenesis at 25°C. (**A**) *nyn-3* gene structure and Zc3h12a ribonuclease domain sequence alignment. Exons (boxes) and introns (lines) are indicated; gray indicates 5′ untranslated region, and light brown corresponds to the Zc3h12a-like ribonuclease NYN domain. Sequence alignment of NYN-3 with Zc3h12a-like ribonuclease NYN domain proteins from different species is shown; *ce*, *Caenorhabditis elegans*; *dm*, *Drosophila melanogaster*; *mm*, *Mus musculus*; *hs*, *Homo sapiens*. The conserved aspartic acid residues are highlighted with a black background. The red asterisks indicate the point mutations in *nyn-3(ht044)* and *nyn-3(ht056)*, and the red line indicates the deletion in *nyn-3(tm2499)* and *nyn-3(ht075)*. (**B**) Brood size counts of WT and *nyn-3* mutants at three different temperatures [****$P < 0.0001$, one-way analysis of variance (ANOVA)]. $n \geq 9$ for all samples. (**C**) Protein expression of various *ha::nyn-3* mutants. Total protein (~100 μg) from various strains grown at 25°C. Wild type indicates *fog-2(q71)*; all the listed mutants are on the *fog-2(q71)* background. The Western blot was probed with anti-HA (top) and anti–glyceraldehyde-3-phosphate dehydrogenase (GAPDH) (bottom) antibodies. MW, molecular weight. (**D**) Brood size counts of mixed and matched crosses between *fog-2(q71)* (wt; yellow), *ha::nyn-3(tm2499);fog-2(q71)* (tm; brown) and *fog-2(q71)* (wt; yellow), *ha::nyn-3(ht044); fog-2(q71)* (ht; blue). (***$P < 0.001$ and ****$P < 0.0001$, one-way ANOVA). ns, not significant. (**E**) Spermatid in vitro activation at 25°C. Left: Spermatozoa of WT and *nyn-3* mutants at 25°C; white arrow indicates pseudopod of the spermatozoa. (**F**) Percentages of in vitro activated sperm containing pseudopods (blue) at 25°C from WT and *nyn-3* mutants. The number of spermatids counted for each mutant is listed above.

brood size were also observed at 15°C, but the severity of the phenotypes was more pronounced at the higher temperature. We saw twofold decreases in the brood sizes of the four *nyn-3* mutants compared to the WTs at 15°C and fivefold decreases at 20°C; however, the effects of the mutations were much more drastic at 25°C [brood sizes of 0 in *nyn-3(tm2499)*, *nyn-3(ht056)*, and *nyn-3(ht075)* and 0.6 in *nyn-3(ht044)*]. Consistent with the notion that defects in *nyn-3* cause sterility, the brood size of *nyn-3 (tm2499)* could be rescued by CRISPR-mediated reintroduction of the deleted fragment back to *nyn-3(tm2499)*; the brood sizes were 93% rescued at 25°C and 100% rescued at 15°C (Fig. 1B).

Quantitation of NYN-3 protein levels in the *nyn-3* mutants revealed that the level of HA::NYN-3(ht044) was comparable to that of WT protein (HA::NYN-3). While the molecular weight of HA::NYN-3(tm2499) is lower than that of the WT protein, the steady-state protein level was comparable. The level of HA::NYN-3(ht056) was low, potentially reflecting an effect on the protein half-life (Fig. 1C).

nyn-3 is essential for spermiogenesis at 25°C

To further dissect whether the temperature-dependent decrease in brood size is associated with defects in sperm or oocyte production

in *nyn-3* mutants, we performed experiments using the *fog-2(q71)* strain (feminization of germ line). In *C. elegans*, hermaphrodites normally produce sperm before producing oocytes. In contrast, *fog-2(q71)* is a feminized hermaphrodite mutant with functional oocytes and no sperm but does not exhibit any apparent defects in spermatogenesis per se. We performed mixed and matched mating of males and feminized hermaphrodites from crosses between *fog-2(q71)* and *nyn-3(tm2499);fog-2(q71)* or *fog-2(q71)* and *nyn-3(ht044);fog-2(q71)*. Brood sizes from these pairings were examined in worms grown at 15°, 20°, and 25°C (Fig. 1D). Only males from the *nyn-3(tm2499);fog-2(q71)* or *nyn-3(ht044);fog-2(q71)* strains produced consistently smaller brood sizes at all three temperatures. Consistent with our previous results, broods from n*yn-3(tm2499)* or *nyn-3(ht044)* males at 15°and 20°C contained between 30 and 60% of the expected number of progenies, but there were almost no progenies produced (brood sizes < 1) when the crosses were performed at 25°C. To eliminate the possibility that the observed sterility was due to a failure of the mutant males to mate at 25°C, we monitored the unfertilized oocytes on the plates as a sign of successful mating.

Since oocyte ovulation requires MSP (major sperm protein) from sperm, our observations of unfertilized oocytes in *nyn-3* mutant derivatives suggested the presence of sperm with sufficient MSP secretion for oocyte ovulation (*15*). We therefore assessed spermatozoa formation upon in vitro activation of spermatids from WT and *nyn-3* mutant lines grown at 25°C. Upon in vitro activation, 92% of spermatids from the WTs formed pseudopods and became motile, while pseudopods were found in less than 10% of spermatids from each of the four *nyn-3* mutants (Fig. 1, E and F). Moreover, since MSP is known to be confined to the region of pseudopod formation, we performed immunostaining of MSP on spermatids from WT, *nyn-3(tm2499)*, and *nyn-3(ht044)* males grown at 15° and 25°C. As expected, MSP in spermatids from all strains grown at 15°C and WTs grown at 25°C were localized at one end of the spermatid. In contrast, MSP staining in spermatids from *nyn-3(tm2499)* grown at 25°C generally showed weak and evenly distributed signal. Intriguingly, MSP protein in *nyn-3(hyt044)* formed a ring around the spermatid (fig. S1B). Nevertheless, mutations in *nyn-3* consistently lead to mislocalization of MSP.

NYN-3 is predominantly expressed in the proximal region of the male gonad and temporally coordinated with ALG-3

To determine the expression pattern of NYN-3, we used the HA antibody to detect the presence of HA::NYN-3 in adult males and feminized hermaphrodites derived from *ha::nyn-3; fog-2(q71)* crosses. Notably, HA::NYN-3 protein was expressed predominantly in males (fig. S1C). Thus, we closely examined the localization of NYN-3 protein in male gonads by immunofluorescence. We examined gonads of *ha::nyn-3; fog-2(q71)* male adult worms and three *nyn-3* mutant derivatives (*ht044*, *tm2499*, and *ht056*) grown at 25°C. Expression of HA::NYN-3 was only detected in the proximal germ line and disappeared rapidly upon spermatid formation (Fig. 2A). While NYN-3 expression was detected in all three *ha::nyn-3* mutants in the proximal germ line, we also still detected signals in the region where spermatids form. This unexpected observation suggested that NYN-3 is tightly regulated upon spermatid formation, but this regulation is somehow lost in all three *nyn-3* mutants (Fig. 2, B to D). Moreover, we also observed defects in chromosome segregation in the spermatids from all *ha::nyn-3* mutants grown at 25°C; unsegregated chromosomes were most prominent in *ha::nyn-3(ht044)* when compared with *ha::nyn-3(tm2499)*, *ha::nyn-3(ht056)*, and *ha::nyn-3(ht075)* lines (Fig. 2, B to E).

Similar phenotypes of temperature-dependent spermatid chromosomal lagging and spermiogenesis defects have been reported for *rrf-3(pk1426)* and mutants associated with *alg-3/4* 26G small RNA biogenesis pathways (*5*, *6*, *10*). Since ALG-3 is known to be localized to the proximal male gonad (specifically to P-granules), we generated *2xflag::alg-3* using CRISPR and compared the localizations of HA::NYN-3 and 2xFLAG::ALG-3 (Fig. 2, D and F). Consistent with the previous studies, ALG-3 was expressed in the proximal germ line, and we further observed cytoplasmic signals for 2xFLAG::ALG-3 and HA::NYN-3 in the proximal gonad. However, the signals for 2xFLAG::ALG-3 were most prominent in the P-granule (*1*), while the signals for HA::NYN-3 were scattered cytoplasmic puncta. The expression level of 2xFLAG::ALG-3 was not obviously altered in *ha::nyn-3(ht056)*, but its disappearance was not as abrupt in the mutant as it was in the WT zone of spermatid formation (Fig. 2D).

NYN-3 is required for the presence of *alg-3/4* 26G small RNAs

To determine whether the levels of *alg-3/4* 26G small RNAs are affected in our *nyn-3* mutants, we performed sequencing of small RNAs from 25°C-grown, male-enriched *ha::nyn-3*(wt), *ha::nyn-3(ht044)* (a catalytically inactive mutant), *ha::nyn-3(tm2499)* (a putative CDA domain deletion mutant), and *ha::nyn-3(ht056)* worms (a hypomorphic mutant with putative CDA domain mutation), all of which were in the 2x*flag::alg-3; fog2(q71)* genetic background. Because we wanted to assess the global changes in small RNAs as well as specific changes in *alg-3/4* 26G small RNAs, we exploited the 5′-monophosphorylated nature of *alg-3/4* 26G small RNAs and prepared two types of small RNA libraries for Illumina sequencing: total small RNAs (total) comprising 5′ cap, tri- and monophosphorylated forms, and only 5′ monophosphorylated (mono) small RNAs.

Consistent with previous studies, 22G small RNAs were predominant in the "total" small RNA libraries, while 21- and 23-nt RNAs with U as the first nucleotide were the major constituents in the "mono" small RNA libraries (Fig. 3A and fig. S2, A to D) (*16*). The 21- and 23-nt RNA populations, respectively, represent 21 U small RNAs and microRNAs. The *alg-3/4* 26G small RNAs were readily observed in *ha::nyn-3* WT samples, but the levels were markedly decreased in all *ha::nyn-3* mutants (Fig. 3A) (*1*).

We then compared the amounts of small RNAs in terms of their target genes, which are categorically determined by the Argonaute protein involved. Excluding microRNAs and 21 U small RNAs, the three major classes of endogenous small RNAs in the male germ line are known as *wagos* 22G, *csr-1* 22G, and *alg-3/4* 26G small RNAs. All three classes of small RNAs are antisense to their targeted coding transcripts; the 22G small RNAs are triphosphorylated at their 5′ terminus, and 26G small RNAs are monophosphorylated at their 5′ end. The class names also indicate the associated Argonaute protein(s) (*1*, *16*, *17*). In the total libraries, neither WAGOs (Worm ArGOnaute proteins) nor CSR-1 (Chromosome-Segregation and RNA interference deficient)–associated 22G small RNAs [25 reads per million (rpm) cutoff] exhibited more than a twofold change in any *nyn-3* mutant compared to WT. In stark contrast, decreases of 10-fold or more were evident for *alg-3/4* 26G small RNAs in all three *ha::nyn-3* mutants (Fig. 3B and table S1). Our data therefore suggest that the ribonuclease activity of NYN-3 is required for proper abundance of *alg-3/4* 26G small RNAs.

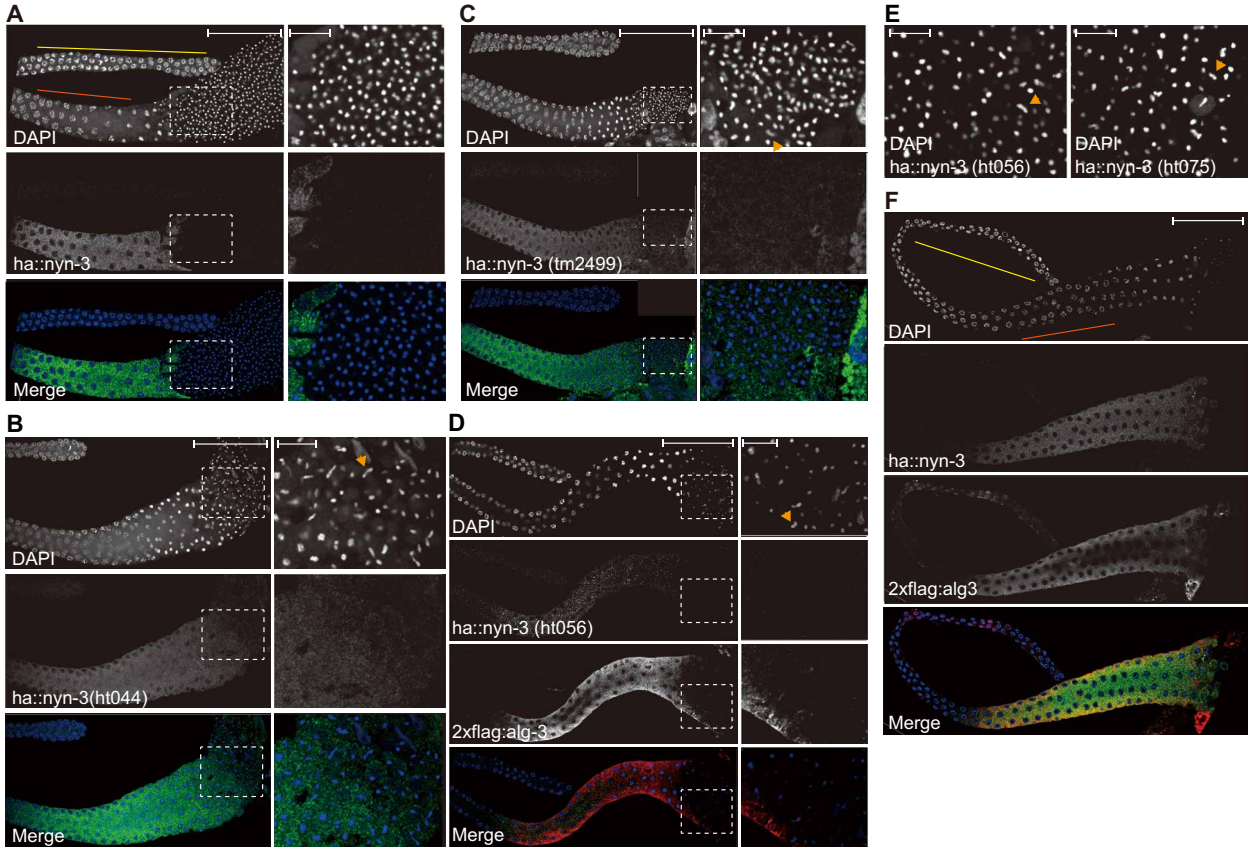

Fig. 2. HA::NYN-3 is expressed in the proximal region of the male gonad and temporally coordinated with 2xFLAG::ALG-3. (**A** to **D** and **F**) Immunostaining of HA::NYN-3 and 2xFLAG::ALG-3 in (A) *ha::nyn-3*, (B) *ha::nyn-3(ht044)*, (C) *ha::nyn-3(tm2499)*, (D) *ha::nyn-3(ht056); 2xflag::alg-3*, and (F) *ha::nyn-3; 2xflag::alg-3*. DNA was stained with 4′,6-diamidino-2-phenylindole (DAPI) (blue), and anti-HA (green) and anti-FLAG (red) staining are shown in the merged image. The spermatid regions are enlarged, and the lagged chromosomes are indicated with an orange arrowheads. (**E**) Image of DAPI-stained spermatids from *ha::nyn-3(ht056) and nyn-3(ht075)*; the lagged chromosome is indicated with an orange arrow. Yellow lines in both *ha::nyn-3* (A) and *ha::nyn-3; 2xflag::alg-3* (F) indicate the distal region of the germ line, and orange lines indicate the proximal germ line. The scale bars in images of whole germ line are 50 μm and in images of spermatids are 10 μm. At least three images are taken for each sample.

Identification of novel *alg-3/4*–targeted genes through 2xFLAG::ALG-3–associated 26G small RNAs

To begin probing the connection between *nyn-3* and *alg-3/4*, we constructed mono small RNA libraries from RNAs in 2xFLAG::ALG-3 immunoprecipitates (IPs). Samples were obtained from male-enriched WTs, three *nyn-3* mutants, and the *rrf-3(pk1426)* line. Consistent with our immunofluorescence imaging of 2xFLAG::ALG-3, the protein levels of 2xFLAG::ALG-3 were similar among all tested genetic backgrounds (Fig. 3C). As in the previous experiments, we constructed total small RNA libraries to determine whether the small RNAs associated with 2xFLAG::ALG-3 were 5'capped/triphosphorylated or monophosphorylated. Consistent with previous observations, ALG-3 was associated with monophosphorylated 26G small RNAs (Fig. 3D and fig. S2, E to G). Confirming our earlier finding that *nyn-3* is important for the abundance of *alg-3/4* 26G small RNAs, we found that monophosphorylated 24- to 27-nt antisense reads from 2xFlag::ALG-3 IP RNAs were markedly reduced compared to WT levels in the *ha::nyn-3(ht044)* (7% of WT levels), *ha::nyn-3(tm2499)* (16%), *ha::nyn-3(ht056)* (17%), and *rrf-3(pk1426)* (0.6%) lines. We normalized the results from IP samples as rpm total reads matched to *C. elegans* genome. Then, we identified ALG-3 targets as those genes with at least twofold enrichment of normalized ALG-3–bound mono antisense small RNAs reads in WTs compared to *rrf-3(pk1426)* (cutoff, 20 rpm in WT). We obtained 1335 genes that are targeted by ALG-3. By comparing our *alg-3* 26G small RNA–targeted gene list with the previously identified *alg-3/4* targets that met that same cutoff, we found that 328 additional genes could be added to the *alg-3/4*–targeted gene list. Among 1008 previous *alg-3/4*–targeted genes that met the cutoff, only one [with a 1.8-fold decrease in *rrf-3(pk1426)* relative to WT] was not present in the our list, suggesting that most if not all previously identified *alg-3/4* targets were detected by our method. Thus, we established a updated *alg-3/4*–targeted gene list by combining the two lists to create a total list of 1736 *alg-3/4*–targeted genes (Fig. 3E and table S2). We then compared the small RNA abundances among the three *nyn-3* mutants, in terms of both total and 2xFLAG:: ALG-3–bound mono small RNAs, by applying the updated *alg-3/4*–targeted gene list. Consistent with our previous observations, all three *nyn-3* mutants exhibited more than 10-fold decreases in *alg-3/4* 26G small RNAs. (Fig. 3F).

Identification of NYN-3–bound RNAs in vivo using ePAR-CLIP

After finding that the ribonuclease activity of NYN-3 is required for normal levels of *alg-3/4* 26G small RNAs, we hypothesized that NYN-3 activity should enhance either the production or the stability of *alg-3/4* 26G small RNAs. To test this hypothesis, we first needed

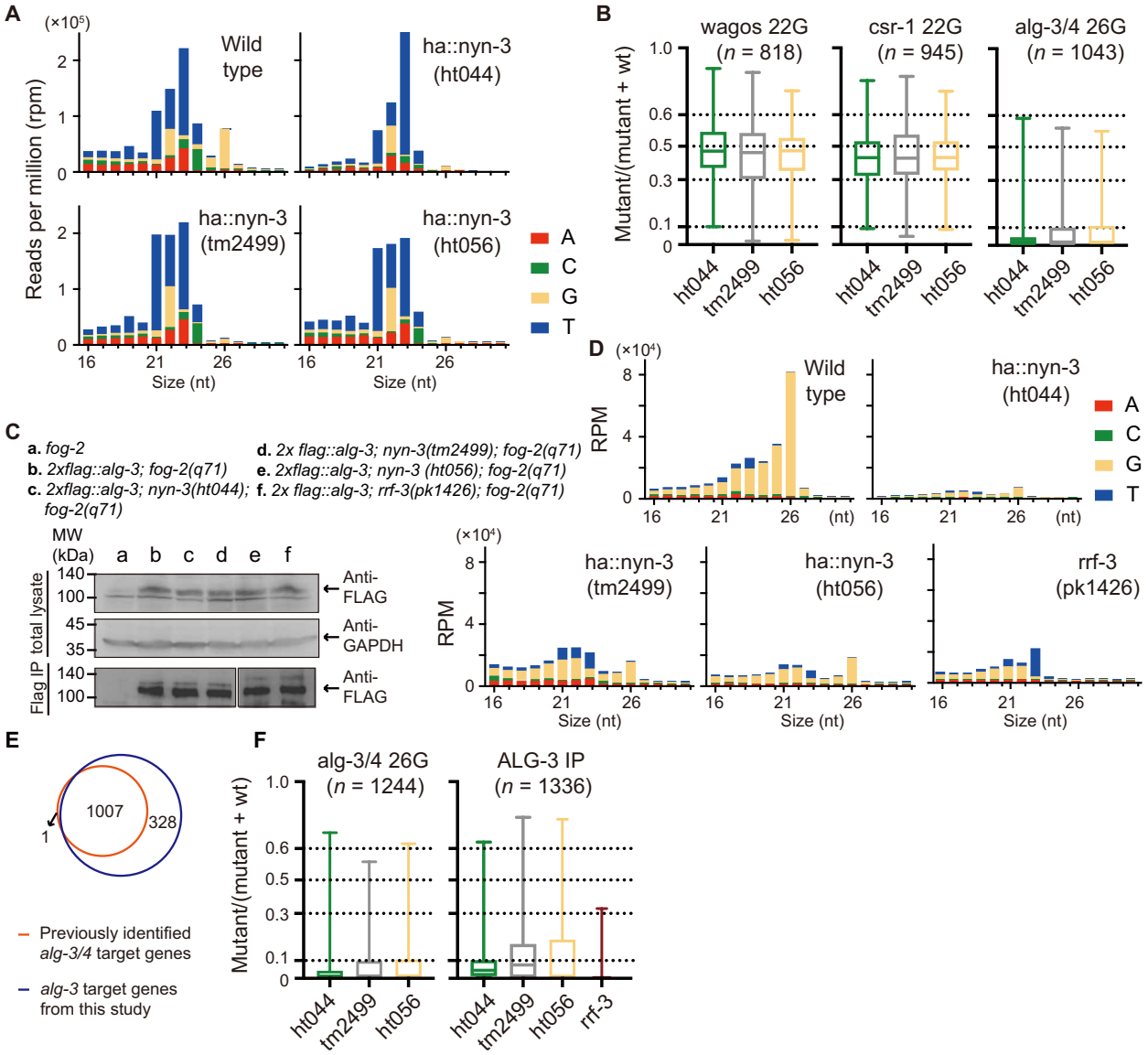

Fig. 3. Differential expression of *alg-3/4* 26G small RNAs and ALG-3–bound small RNAs in *nyn-3* mutant derivatives. (**A** and **D**) Sizes and first nucleotide distributions of monophosphorylated total small RNA (A) and 2xFLAG::ALG-3–immunoprecipitated (IPed) (D) libraries. (**B**) Relative abundances of small RNAs in *wagos*, *csr-1*, and *alg-3/4* classes of genes from total male-enriched small RNAs. The *y* axis indicates mutant/(mutant + WT), and the three dashed lines indicate 2-fold increases (0.6), 2-fold decreases (0.3), and 10-fold decreases (0.1). The numbers of genes meeting the cutoff and analyzed in each category are labeled. (**C**) Protein expression of 2xFLAG::ALG-3 in *fog-2(q71)*, *rrf-3(pk1426)*, and various *ha::nyn-3* mutants. Top: 2xFLAG::ALG-3 was detected in total lysate (100 μg); GAPDH served as a loading control. Bottom: 2xFLAG::ALG-3 IP confirmation for the 2xFLAG::ALG-3–IPed small RNA libraries. (**E**) Overlap between the newly identified *alg-3*–targeted genes (blue) and preexisting *alg-3/4*–targeted genes that met the cutoff (orange). (**F**) Relative abundances of small RNAs in updated *alg-3/4* target genes from male-enriched (left) and 2xFLAG::ALG-3–IPed (right) small RNAs.

to determine the identities of NYN-3–targeted RNA substrates. Thus, we took advantage of the specific and enhanced cross-linking efficiency of PAR-CLIP (photoactivatable ribonucleoside–enhanced cross-linking and immunoprecipitation) (*18*). This method was further modified to incorporate improved library preparation and enhanced cloning efficiency [eCLIP, enhanced ultraviolet (UV) cross-linking, and IP] (*19*); the improved method is called ePAR-CLIP. We performed ePAR-CLIP studies using catalytically inactive *ha::nyn-3(ht044)*. One input and two independent HA-IP samples from male-enriched *ha::nyn-3(ht044)* lysates were analyzed. The quality of our ePAR-CLIP sequencing (ePAR-CLIP-seq) data was evaluated according to established CLIP-seq data analysis protocols (https://galaxyproject.github.io/training-material/topics/transcriptomics/tutorials/clipseq/tutorial.html) using Galaxy/CLIP-Explorer (https://clipseq.usegalaxy.eu). After matching to the *C. elegans* genome (ce10) using RNA STAR and removing overrepresented polymerase chain reaction (PCR) products with the UMI (Unique Molecular Identifiers)–tools deduplicate program, we obtained 2,293,311 sequences for the input, 321,312 sequences for the IP1 sample, and 484,859 sequences for the IP2 sample. Our correlation analysis showed that IP1 and IP2 were well correlated and distinct from the input (Fig. 4A).

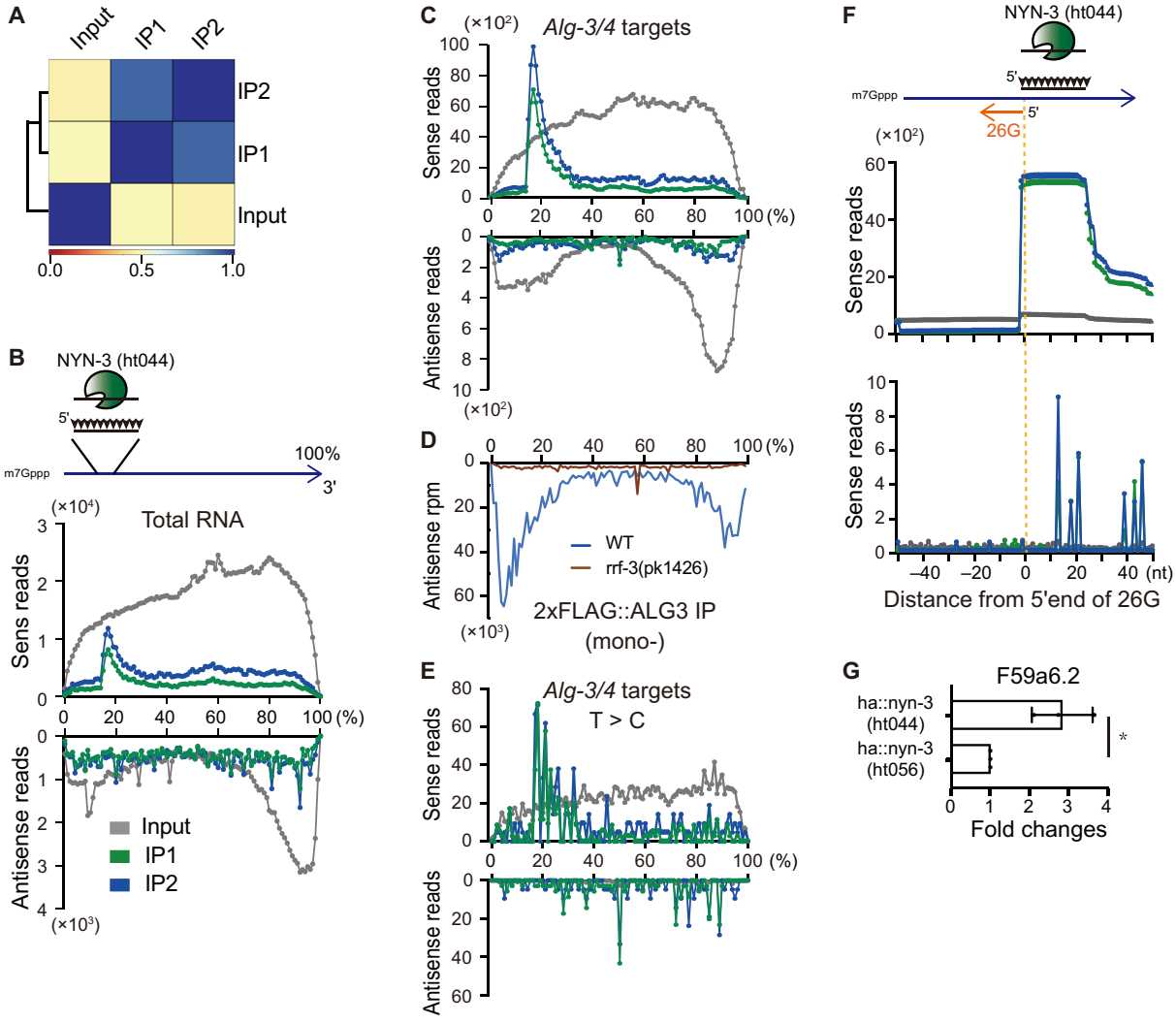

Fig. 4. HA::NYN-3 (ht044) ePAR-CLIP analysis. (**A**) Sequence data correlation between one input and two HA-IP samples, derived from plotCorrelation program from Galaxy/CLIP-Explorer. (**B**, **C**, and **E**) Distribution analysis of ePAR-CLIP reads along total coding transcripts and pseudogenes (B), *alg-3/4*–targeted genes (C), and T to C mutation sites (E). The sense reads are shown on top and antisense reads are shown below. (**D**) Distribution analysis of the amount in rpm of antisense monophosphorylated small RNAs from 2xFLAG::ALG-3 IP from WT (blue) and *rrf-3(pk1423)* (brown). (**F**) Relative position of ePAR-CLIP reads (top) and T to C mutations (bottom) corresponding to 5′ regions of the most abundant antisense reads in individual genes from monophosphorylated 2xFLAG::ALG-3–IP small RNA. The number of reads was normalized to reads per 100,000 total reads. (**G**) HA::NYN-3(ht044) RNA IP relative to HA::NYN-3(ht056) RNA IP and quantitation of *f59a6.2* mRNA using reverse transcription quantitative PCR (RT-qPCR).

To match our ePAR-CLIP results to cDNAs, we performed a distribution analysis of ePAR-CLIP reads against total coding transcripts. The distribution analysis was performed to assess the density of every position of ePAR-CLIP–normalized reads along the reference genes; gene length was normalized. Since our minimal read count was 321,312 (IP1 sample), the normalization entailed counting the read number per 100,000 total reads matched to the *C. elegans* genome. The distribution analysis on the total reads from ePAR-CLIP suggested that the majority of reads from the two IP samples were sense reads enriched at 17 to 30% from the 5′ end of coding transcripts (Fig. 4B). Since our previous results showed that functional NYN-3 is necessary for proper abundance of *alg-3/4* 26G small RNAs, we performed the distribution analysis using the updated list of *alg-3/4*–targeted coding transcripts as reference genes. The enrichment of the sense peak was even more prominent in both IP samples and still enriched at 16 to 30% of *alg-3/4*–targeted coding transcripts (Fig. 4C). To understand how NYN-3 may support *alg-3/4* 26G small RNA abundance, we compared the relative distributions of NYN-3(ht044)–associated RNAs from ePAR-CLIP-seq and the distributions of 5′ end position of ALG-3–bound 26G small RNAs among the *alg-3/4*–targeted transcripts. We observed that the ALG-3–bound 26G small RNAs were enriched at both 5′ and 3′ termini of the transcripts, ranging from 2 to 26% and 84 to 98% from the 5′ end of *alg-3/4*–targeted coding transcripts. (Fig. 4D) However, we did not observe *ha::nyn-3(ht044)* ePAR-CLIP read enrichment at the 3′ end of *alg-3/4*–targeted coding transcripts. This result could be due to the high potential for *ha::nyn-3(ht044)* ePAR-CLIP reads at the 3′ end to contain poly(A) regions. Hence, insufficient 4-thiouridine (4-thio-U) incorporation would artificially dampen reads. Since T to C changes have been reported in the final

sequencing data when 4-thio-U–cross-linked samples were sequenced, we also performed the distribution analysis on the T to C mutations in the *alg-3/4*–targeted genes. Consistent with the distribution analysis on reads, the most predominant enrichments of T to C mutations were at sense reads within 18 to 33% positions from the 5′ end of coding transcripts (Fig. 4E). To determine how exactly these ePAR-CLIP reads correlate with *alg-3/4* 26G small RNAs at the nucleotide level, we again used the 5′ ends of the most abundant antisense reads from WT 2xFlag::ALG-3–bound mono small RNAs as the reference position 0 and summed up the ePAR-CLIP reads that were present 50 nt upstream or downstream of the reference position in all the *alg-3/4*–targeted genes. We were excited to find a strong cumulative enrichment of sense reads downstream of the reference position, at the 5′ end of the most abundant 26G small RNAs. Furthermore, the T to C changes were also enriched downstream of the reference point. Our *ha::nyn-3(ht044)* ePAR-CLIP data therefore suggest that HA::NYN-3(ht044) binds to sense mRNA transcripts immediately downstream of the corresponding antisense 26G RNA initiation sites (Fig. 4F).

To cross-validate the ePAR-CLIP data, we performed RNA IP using *ha::nyn3(ht044)*. The hypomorph mutant, *ha::nyn-3(ht056)*, was used as a negative control. The most prominent target from ePAR-CLIP data, the *f59a6.2* transcript, was further detected using reverse transcription quantitative PCR (RT-qPCR). Since NYN-3 is localized to the cytoplasm, the NYN-3–targeted RNAs are expected to be mature mRNAs. Therefore, we designed one of the qPCR primers to target the exon-exon junction. Consistent with our ePAR-CLIP data, we were able to detect a 2.84-fold average enrichment of *f59a6.2* spliced mRNA in the HA::NYN-3(ht044) IP relative to HA::NYN-3(ht056) IP (Fig. 4G).

Since our ePAR-CLIP data suggested that NYN-3(ht044) recognizes *alg-3/4*–targeted mRNAs at a site approximately 50 nt downstream of the initiation site in abundant 26G small RNAs, we were curious whether we could identify a specific NYN-3 recognition sequence motif. We filtered peaks called by the PEAKachu peak calling program and then performed a MEME motif search in the *alg-3/4*–targeted genes (fig. S3A, bottom). In addition, we performed a MEME search on sequences 50 nt downstream of the most abundant 26G small RNA initiation sites, probing *alg-3/4*–targeted genes that were at least 10 rpm among the most abundant *alg-3/4* 26G small RNAs (fig. S3A, top). Using the TOMTOM program to determine the overlap in the search results from these two exercises, we identified an AG-rich motif with a *P* value of 0.0000381, which was much lower than the minimal *P* value of 0.041 when the search results were overlapped with 50 randomly selected nucleotides from the first 30% of non–*alg-3/4*–targeted genes (fig. S3B). The strong overlap was consistent with our finding that HA::NYN-3(ht044)–associated RNAs were enriched 50 nt downstream of *alg-3/4* 26G small RNA target sites. However, the identified AG-rich motif was only present in 273 of 1688 genes, according to the criteria that the motif is at least 8-nt long and downstream of the most abundant 26G small RNAs. Thus, the identified motif is not especially likely to be recognized by NYN-3. Catalytically inactive NYN-3 can trap RNA substrates. However, unlike most Zc3h12a-like ribonuclease proteins in mammals that contain an RNA binding domain, NYN-3 does not contain any known RNA binding domain or motif, and RNA substrate recognition is not likely to be a direct function of NYN-3 (*20*).

Overall, our ePAR-CLIP-seq data showed that HA::NYN-3(ht044) mainly associates with mRNAs just downstream of corresponding *alg-3/4* 26G small RNA initiation sites. This finding suggests that NYN-3 is likely to be functionally involved in creating templates for RRF-3 that ultimately lead to *alg-3/4* 26G small RNA biogenesis.

HA::NYN-3 IP 3′ RACE assay and identification of HA::NYN-3 cleavage site(s)

After concluding that catalytically inactive HA::NYN3(ht044) binds to mRNAs downstream of the corresponding antisense 26G small RNA initiation sites, we next wanted to identify the NYN-3 cleavage site(s) on the mRNAs. To do so, we performed 3′ rapid amplification of cDNA ends (RACE) on RNAs that were immunoprecipitated (IPed) with HA::NYN-3. Briefly, we used global 3′ ligation to capture the 3′ termini of HA::NYN-3-IP RNAs, and then we used nested PCRs to sequentially enrich for genes of interest before polyacrylamide gel electrophoresis (PAGE) analysis or Illumina sequencing (*13*). The RNA products cleaved by NYN-3 are expected to have lower affinity than the RNA substrates, so we relied on 4-thio-U–mediated cross-linking to capture these RNAs. We then specifically amplified the region around the cleavage site on *f59a6.2* mRNA. We focused on this target mRNA for three reasons: (i) It was detected in HA::NYN-3(ht044) RNA IP; (ii) it is complementary to the most abundant ALG-3–bound 26G small RNAs; and (iii) most of the reads obtained from ePAR-CLIP-IP samples corresponded to this mRNA. By analyzing the ALG-3–bound 26G small RNA distribution on *f59a6.2*, we found two adjacent major 26G small RNA peaks that were separated by 24 nt, which is consistent with the previously described model of 26G small RNA amplification (*6*). Since both of the ALG-3–bound 26G small RNAs on *f59a6.2* were absent in all the *nyn-3* mutants tested, we reasoned that the initial cleavage by NYN-3 should be downstream of the second peak (Fig. 5A, fig. S3C, and Discussion). Thus, the PCR amplicon that we targeted in the following analysis lies between the 3′ adaptor and the downstream major 26G small RNAs. Moreover, the position corresponding to 5′ end of this 26G small RNA was taken as "0" for the purposes of labeling consistency (Fig. 5A).

We first performed HA::NYN-3–IPed *f59a6.2* 3′ RACE on WTs and *ha::nyn-3(ht044)* mutants (the catalytically inactive mutant). The *rrf-3(pk1426)* mutant without *ha* tagging on *nyn-3* served as a negative control. On the basis of our ePAR-CLIP data, if the RNA fragments are cleaved by NYN-3, then we expect that the size of RT-PCR amplicons should be between 0 and 24 bp plus adaptors, corresponding with the stretch of nucleotides from the downstream 26G small RNA to the 50th position from the 5′ end of the most abundant 26G (26 nt). Thus, we suspect that bands above 24 bp represent RNA substrates that were cross-linked to NYN-3 but had not been cleaved by NYN-3, whereas the amplicons below 24 bp should represent the cleaved RNA products.

We further compared RT-PCR amplicons derived from *ha::nyn-3* and *ha::nyn-3(ht044)*, the ribonuclease catalytic defective mutant. Notably, *ha::nyn-3(ht044)* samples had a 1.2-fold enrichment of amplicons above 24 bp (relative to the intensity of the entire lane) compared to *ha::nyn-3*. In addition, two regions showed potential cleavage patterns in *ha::nyn-3*, and these regions were distinct or decreased in *ha::nyn-3(ht044)*. We observed a band at 17 to 26 bp and four continuous bands between 7 and 12 bp, which were evenly distributed in WT; only the highest molecular weight band was enriched in *ha::nyn-3(ht044)*. In addition, both the cleaved and uncleaved amplicons were higher than in the negative control (Fig. 5B). To test whether the amplicons that we observed on native PAGE were real, we confirmed the identities of the amplicons (within *f59a6.2*)

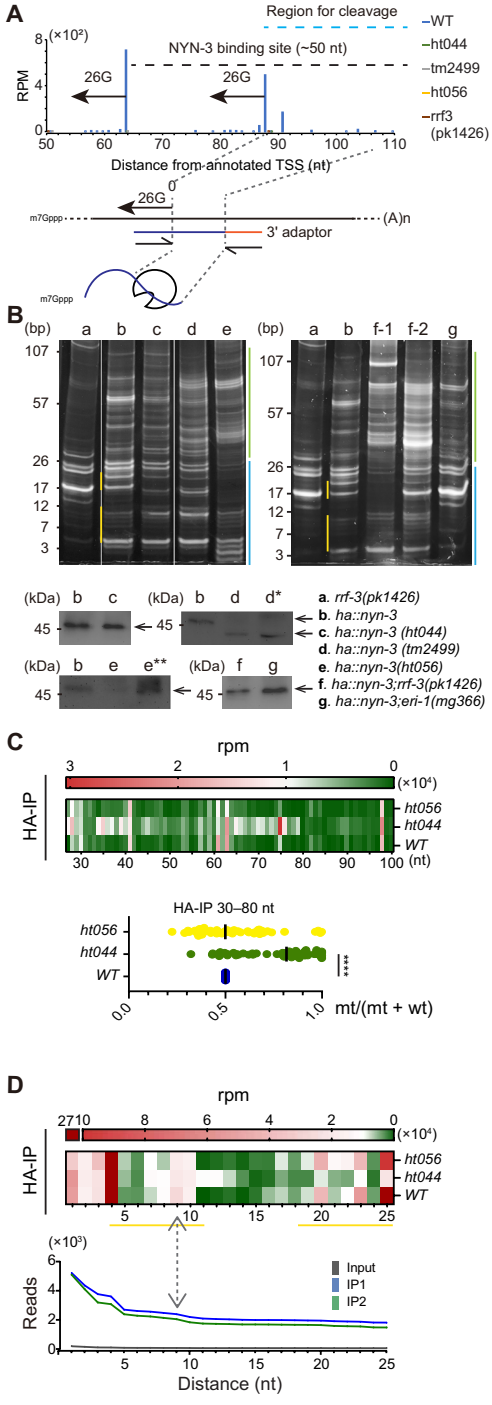

Fig. 5. 3′ RACE on HA::NYN-3–IPed RNAs from *nyn-3* mutants. (**A**) Experimental design of 3′ RACE on HA::NYN-3–associated *f59a6.2*. Top: *f59a6.2* 26G small RNA distribution along the gene; the quantities and positions of 5′ end of 26G small RNAs (blue vertical lines) and the NYN-3 binding site from ePAR-CLIP-seq data (black dashed line) and possible NYN-3 cleavage sites (light blue dashed line). Bottom: Primer design for the final PCR amplicons derived from HA::NYN-3–bound RNAs. (**B**) HA::NYN-3–IPed *f59a6.2* 3′ RACE RT-PCR amplicons from various genetic backgrounds. Male-enriched protein lysate (10 mg) from each strain was used for HA-IPed 3′ RACE cloning. Top: Separating PCR amplicons on 22% 1× tris-borate EDTA (TBE)–PAGE. Differently colored lines at the right side of gel image indicate the sizes of PCR amplicons corresponding to 3′ end of RNA, either within (blue) or further away (green) from the expected NYN-3 binding site. Yellow lines within image or in (D) indicate the observed cleavage sites. Bottom: Probing HA::NYN-3 in HA::NYN-3 IP samples from the top using anti-HA antibody; samples were 250-μg IP from male-enriched lysates, except that "*" had twice, and "**" had fivefold the amount. HA::NYN-3 is indicated by arrows. (**C** and **D**) Heat plots represent the Illumina sequencing results of HA::NYN-3 bound, 3′ end of *f59a6.2* RNAs from WT, *nyn-3(ht044)*, and *nyn-3(ht056)*. (C) Normalized reads of RNA fragments larger than expected NYN-3 cleavage site (>30 nt, as described in the text) and the fold changes of same length fragments among different strains. mt, wt: rpm in samples from mutants and WTs, respectively. (D) Normalized reads of RNA fragments within the expected NYN-3 cleavage sites (top) and the ePAR-CLIP-seq data of *f59a6.2* at the corresponding region are shown (bottom). Gray arrow indicates the NYN-3 cleavage site (****$P < 0.0001$).

using manual sequencing and Illumina sequencing (Fig. 5, C and D, table S3).

In the 2 to 10 million sequences that we obtained from each sample set, the average length downstream of 26G small RNA primer sites was ~33 nt in HA::NYN-3(ht044) IP and ~23 nt in HA::NYN-3 IP samples. These findings are consistent with our other data and the idea that HA::NYN-3(ht044) should bind and protect the RNAs, allowing it to retain the longer RNA fragments (table S4).

We then summed up the reads based on their 3′ end position on *f59a6.2* transcripts and normalized to total reads for each sample to see whether the sequencing result is consistent with the PAGE analysis. Encouragingly, *f59a6.2* fragments longer than 30 nt from 5′ end of 26G small RNA were specifically enriched in *ha::nyn-3(ht044)*, and the enriched long RNAs were even observed up to 80 nt downstream of the 5′ end of 26G small RNA (Fig. 5C, top). A significant enhancement in normalized reads was also observed when comparing the fold change of *ha::nyn-3(ht44)* to *ha::nyn-3* at the same size RNA fragments from 30 to 80 nt from the 5′ end of 26G small RNA (Fig. 5C, bottom). The potential cleavage sites that we found on PAGE were also detected in our sequencing results (Fig. 5D). Despite the nonspecific bands observed on PAGE (17 to 26 bp), the ninth nucleotide downstream of the 5′ end of 26G small RNA was specifically enriched in the WT. We further correlated the NYN-3 cleavage site on *f59a6.2* with previous ePAR-CLIP data on *f59a6.2* (Fig. 5D, bottom). Consistent with our results, there was a strong enrichment of ePAR-CLIP reads from both IP samples surrounding the NYN-3 cleavage site (Fig. 5D). Previous characterization of the RNA substrates for the Zc3h12a in mouse, Regnase-1, showed that the stem-loop structure is often present in the substrates, and the single-stranded loop region is the preferred Regenase-1 cleavage site (*21*, *22*). Next, we predicted the secondary structure surrounding the NYN-3 binding/cleavage site of *f59a6.2* (fig. S4A). The secondary structures predicted based on minimal free energy contained stem-loop structures (*23*, *24*). However, the cleavage site on *f59a6.2* mRNA is 2 nt within the stem. Whether this unexpected cleavage location is due to a potential interacting protein that facilitates RNA binding of NYN-3 or if there is a difference between the predicted and authentic secondary structure of the RNAs will require further study.

HA::NYN-3 associates with *alg-3/4*–targeted transcripts before RRF-3, and three *ha::nyn-3* mutants are capable of binding to RNA substrates

Since we were able to confirm our HA-IP PAGE results showing longer RT-PCR amplicons with Illumina sequencing, we next performed RT-PCR on HA-IP samples from the other two *nyn-3* mutants, *ha::nyn-3(tm2499)* (a putative CDA domain deletion mutant) and *ha::nyn-3(ht056)* (a hypomorphic CDA mutant), to check whether either was capable of binding *f59a6.2* RNA. An apparent enhancement in the intensity of RT-PCR amplicons above 26 bp was observed in both *nyn-3* mutants compared to the negative control, suggesting that both *ha::nyn-3(tm2499)* and *ha::nyn-3(ht056)* are capable of binding to *f59a6.2* transcripts (Fig. 5B). Since we found that the protein level of *ha::nyn-3(ht056)* was low in total worm lysates, we increased the of *ha::nyn-3(ht056)* HA-IP input by fivefold; in doing so, we probed comparable amounts of HA::NYN-3(ht056) and HA::NYN-3 by IP. Notably, our results suggested that we were able to successfully IP HA::NYN-3(ht056). Moreover, although it took more cycles to amplify the associated RNAs than it took for the WT, the mutants are still capable of associating with *f59a6.2* transcripts. Because of the instability of HA::NYN-3(tm2499) after IP, we used twice the amount of HA::NYN-3(tm2499) relative to HA::NYN-3 (Fig. 5B, bottom, and table S3). Together, these data suggest that all three NYN-3 mutant derivatives are capable of binding to its RNA substrates.

The ERI/DICER complex is known to be involved in *alg-3/4* 26G small RNA production. To determine whether targeted RNA binds to HA::NYN-3 before the ERI/DICER complex, we generated *ha::nyn-3;eri-1(mg366)* and *ha::nyn-3;rrf-3(pk1426)* strains and performed HA-IP *f59a6.2* 3′ RACE. Consistent with the hypothesis that NYN-3 cleaves the RNA to create a template for RRF-3, we observed a strong accumulation of *f59a6.2* transcripts associated with HA::NYN-3 in *ha::nyn-3;rrf-3(pk1426)*. The intensities of *f59a6.2* amplicons above 26 bp that were associated with HA::NYN-3 in *ha::nyn-3*; *eri-1(mg366)* were comparable to those in WT, *ha::nyn-3*. (Fig. 5B and table S3). Overall, these results were consistent with our model that *alg-3/4*–targeted transcripts associate with HA::NYN-3 before RRF-3 and ERI-1.

No C to T changes are associated with the putative CDA domain

Since we were able to identify the cleavage site of NYN-3 by comparing 3′ RACE results between HA-IPs from *ha::nyn-3* and *ha::nyn-3(ht044)*, we next performed a similar 3′ RACE on HA-IPs from *ha::nyn-3(ht056)*. The HA-tagged protein level was low in *ha::nyn-3(ht056)* strain, which carries mutations in the only conserved amino acids in the putative CDA motif. Our data suggested that the HA-IP is capable of capturing the low-abundance HA::NYN-3(ht056) (20% of the WT level). Thus, we reasoned if there is CDA activity associated with NYN-3, we should be able to identify differences in C to T changes comparing the HA-IP 3′ RACE results from *ha::nyn-3* and *ha::nyn-3(ht056)* strains. The Illumina sequencing results on RNA fragments bound to HA::NYN-3(ht056) revealed that neither overall nor individual C to T changes were enriched in WTs compared to *nyn-3(ht056)* (fig. S4, B and C). Therefore, our results suggest that the putative CDA motif in NYN-3 is not likely to be a functional CDA.

Identification of RNA templates for 26G small RNA from ALG-3–bound sense RNA

We next wanted to determine whether there are specific rules that guide the placement of adjacent ALG-3–bound 26G small RNAs and their corresponding sense RNAs, which are likely to be the template strands for *alg-3/4* 26G small RNAs. Therefore, we defined the 5′ end of the most predominant antisense 5′-monophosphorylated small RNA from WT 2xFLAG::ALG-3 IP in each *alg-3/4*–targeted gene as reference (position 0) and tabulated the reads within 50 nt upstream and downstream from the reference position. Consistent with earlier studies, we observed phased sense and phased antisense reads from 5′-monophosphorylated 2xFLAG::ALG-3 IP RNAs. The phased antisense 26G small RNAs had 5′ ends 24 nt from the adjacent antisense 26G small RNAs (2-nt overlap). Phased 22-nt sense small RNAs, which are complementary from −22 to −1 position (or +1 to +22) of 26G small RNAs, were also observed in the 2xFLAG::ALG-3 IP mono small RNA libraries. As expected, these signature reads were absent in all the *nyn-3* and *rrf-3* mutants (fig. S5A) (*6*).

Since the phased sense small RNAs were monophosphorylated (as would be expected for Dicer products), we were interested to identify the original sense RNA that served as a template for *alg-3/4* 26G small RNA production. Therefore, we searched the sense RNAs from 2xFLAG::ALG-3 IP total small RNA libraries for those with a

length spanning the entire 26G small RNA. When comparing the relative abundances of these RNAs in *rrf-3(pk1426)* and *ha::nyn-3(ht044)*, the NYN-3 catalytic defective strain, we found significantly more ALG-3–bound sense RNAs in WTs than in *ha::nyn-3(ht044)* and *rrf-3(pk1426)* strains (Fig. 6A); this observation is consistent with NYN-3 ribonuclease function upstream of RRF-3. Moreover, most of the 5′ positions of ALG-3–bound templating sense RNAs from the total RNA library were identical for each gene, regardless of the genotype analyzed, i.e., WT, *ha::nyn-3(ht044)*, or *rrf-3(pk1426)*. Since the RNAs are absent in the mono ALG-3–bound sense RNA libraries, it is reasonable to expect that the 5′ ends of these RNAs are likely capped or triphosphorylated (fig. S5B). Since the RNA templates for *alg-3/4* 26G small RNAs are thought to be mRNAs, we next examined whether the 5′ ends of capped/triphosphorylated ALG-3–bound sense RNA are identical to the capped positions of the respective mRNAs, according to previous cap-seq data (*25*). Intriguingly, the 5′ ends of capped/triphosphorylated ALG-3–bound sense RNA were mostly downstream of the identified cap sites (median, 36 nt downstream), suggesting that the transcript serves as the RNA template for 26G small RNA production has alternative transcription start sites (TSSs) (Fig. 6B and table S5). Of note, the cap-seq was done in hermaphrodites, while our 2xFLAG::ALG-3 IP was done in males, leaving open the possibility that the results were biased by sex. By analyzing ePAR-CLIP input sample of T27A3.4, we found that abundant reads initiate the same position as capped/triphosphorylated ALG-3–bound sense RNAs, but 50 nt downstream of the capped position of mRNA identified from cap-seq suggests that the alternative TSSs are likely male specific (fig. S5C).

We next performed the MEME motif search using the sequence between the capped/triphosphorylated ALG-3–bound sense RNAs and 50 nt downstream of the major peak of 26G small RNAs. An AG-rich motif (WHYRTYGMARHTGHHGRAGGW) was found in all 48 sequences that met the criteria (5 read cutoff in ALG-3–bound total sense RNAs and 10 read cutoff in major peak of ALG-3–bound 26G small RNAs), with an *E* value of 1.0×10^{-12} (fig. S5D, top). To examine the specificity of the identified motif, we also performed a MEME search on sequences randomly selected from 48 size-matched non–*alg-3/4*–targeted sequences from the first 15% of genes. No significant motif was found. However, a somewhat similar motif (WHYDTYBMARHTKHHGRA, *E* value = 6.21×10^{-7}) could only be found in all the *alg-3/4*–targeted genes if the stringency of most abundant 5′ end of 26G small RNA peak was above 20 reads (fig. S5D, bottom). Our search suggests that *alg-3/4*–targeted mRNA recognition is likely mediated by the sequence between the TSS and 26G small RNAs site.

Distinct roles of *alg-3/4* 5′– and *alg-3/4* 3′–targeted 26G small RNAs

It is known that *alg-3/4* 26G small RNAs are essential for spermiogenesis at 25°C, but how these small RNAs regulate gene expression and whether there are differential distributions of *alg-3/4* 26G small RNAs in *nyn-3* mutants remain open questions. To address these questions, we performed distribution analysis on antisense small RNAs from total and 2xFLAG::ALG-3 IP mono small RNA libraries derived from WTs and *nyn-3* mutants (Fig. 6, C and D). We observed *alg-3/4* 26G small RNAs at both the 5′ and 3′ termini of transcripts, with a bias toward the former in the 2xFLAG::ALG-3 IP samples. Moreover, the 26G small RNAs in *ha::nyn-3(ht044)* were generally absent, regardless of the targeted terminus. The 26G small RNAs targeting the 5′ termini of mRNAs were also severely depleted in both *ha::nyn-3(tm2499)*

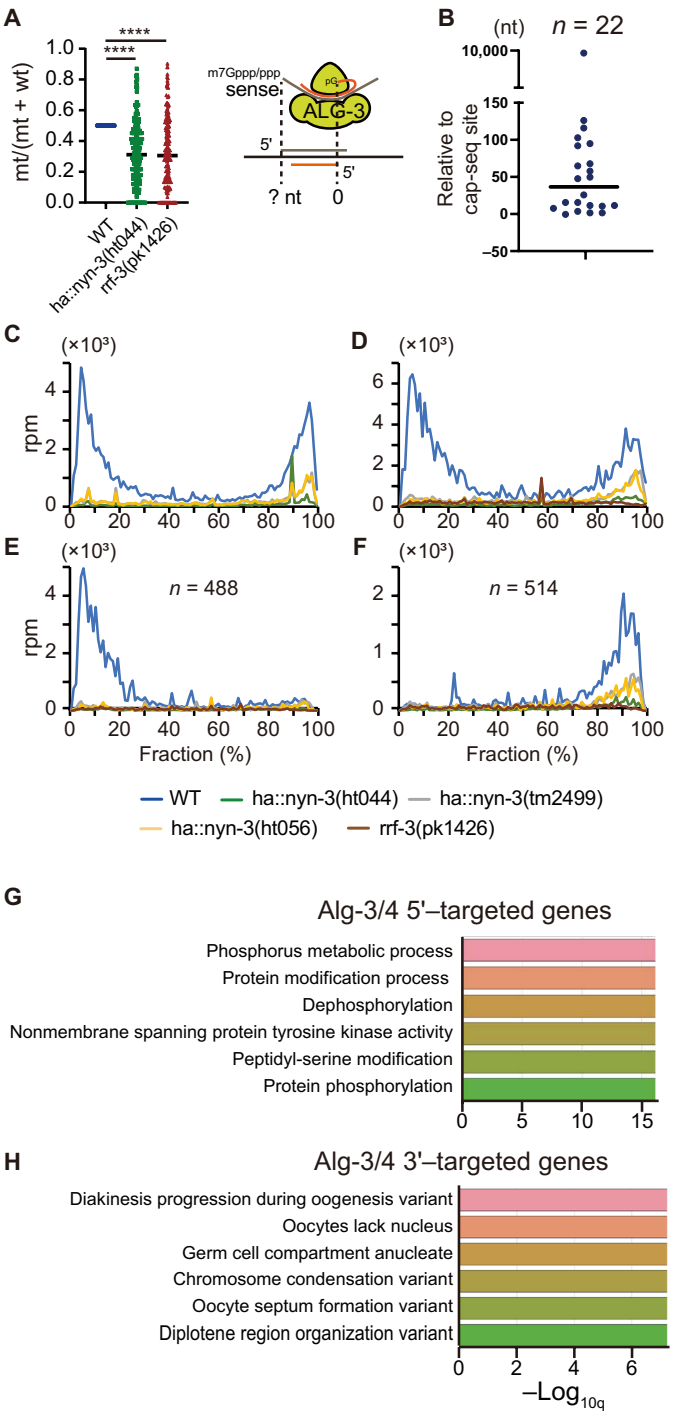

Fig. 6. Categories of ALG-3–bound small RNAs. (**A**) The relative abundance of ALG-3–bound sense templating small RNAs from total RNA libraries with normalized reads in gene (10-rpm cutoff) in WTs. (**B**) Relative position of 5′ end of the most abundant sense read to TSSs identified from cap-seq. (**C** to **H**) Analysis of *alg-3/4* 5′– and *alg-3/4* 3′–targeted 26G small RNAs. (C and D) Distribution analysis of the amount (rpm) of 5′ ends of antisense monophosphorylated small RNAs from total (C) and 2xFLAG::ALG-3 IP (D) RNAs from WT and all *nyn-3* mutants. (E and F) The distributions of 5′ (E) and 3′ (F) termini of 26G small RNAs from monophosphorylated 2xFLAG::ALG-3 IP. (G and H) Results of Gene Ontology analysis of *alg-3/4* 5′–targeted genes and phenotype enrichment analysis of *alg-3/4* 3′–targeted genes.

and *ha::nyn-3(ht056)* strains, while there was only a modest twofold decrease of 26G small RNAs that target 3′ termini (Fig. 6D).

We then further investigated the differences between genes regulated by 5′- and 3′-targeted 26G small RNAs. The genes were grouped on the basis of whether their corresponding 26G small RNAs targeted to 5′ or 3′ termini, using the criteria that the normalized read counts for the first or last one-fifth of the gene should be at least twofold more abundant than the normalized read count of the other terminus. We identified 488 genes with 5′-targeted 26G small RNAs and 514 genes with 3′-targeted 26G small RNAs (table S6). Subsequently, we performed small RNA distribution analyses on these two sets of genes (Fig. 6, E and F). Consistent with the results from our previous analysis, the small RNAs that were depleted at either terminus corresponded to the established inventory of genes.

We next performed enrichment analyses on the *alg-3/4* 3′– and 5′–targeted genes. As expected, results from tissue enrichment analysis showed that the genes are enriched in males and in the germ line, with 5′-targeted genes most enriched in the male and 3′-targeted genes most enriched in the germ line. The Gene Ontology enrichment analysis of the 5′-targeted genes revealed genes related to protein (de)phosphorylation (e.g., phosphorus metabolic processes, protein modification process, and dephosphorylation). In contrast, the phenotype enrichment analysis revealed that 3′-targeted genes are often related to defects in chromosome organization (e.g., diakinesis progression during oogenesis variant, oocytes lack nucleus, germ cell compartment anucleate, etc.) (Fig. 6, G and H). These findings allowed us to make generalizations about the functions of *alg-3/4*–targeted genes and may help to explain the chromosome segregation defects seen in mutants without 26G small RNAs. Although we found chromosomal segregation defects in three *nyn-3* mutants, longer chromosomes were more prominent in *ha::nyn-3(ht044)* than in *ha::nyn-3(tm2499)* and *ha::nyn-3(ht056)* (Fig. 2). Protein phosphorylation has long been known to participate in various steps of spermatogenesis, including meiosis, differentiation, and transformation during spermiogenesis. For example, MAPKs (mitogen-activated protein kinases) are required for sperm development in mouse, and a testis-specific serine/threonine (tssk) protein family is also known to be involved in spermiogenesis (*26*, *27*).

A previous study identified both mRNAs and proteins that are positively or negatively regulated by *alg-3/4* 26G small RNAs. To test whether *nyn-3* mutants also exhibit changes in mRNAs and proteins, we detected the levels of mRNAs from four genes and the levels of MSP. The results were then compared with previously published data (*5*, *6*). The changes in mRNA quantities were largely similar to those identified from previous mRNA sequencing data, and the levels of MSP corresponded to previous mass spectrometry data (fig. S5, E and F). Overall, our data showed that the mRNA and protein decreases known to occur in *alg-3/4* double mutants (compared to WT) are similarly found in *rrf-3 (pk1426)* and three *nyn-3* mutants (*ht044*, *tm2499*, and *ht056*). We also tested the potential correlation between *alg-3/4* 5′– or 3′–targeted 26G small RNAs and directional effects on gene regulation. There was no overall distribution bias toward up-regulation or down-regulation of mRNAs in mutants with diminished 26G small RNAs (fig. S5, G to I). Our distribution analysis revealed a stronger bias in the proteins regulated by 26G small RNAs associated with *alg-3/4* 5′– and *alg-3/4* 3′–targeted 26G small RNAs (fig. S5, J and K). Similar numbers of genes with their proteins were regulated by 5′- and 3′- targeted *alg-3/4* 26G small RNAs. However, two-thirds (54 of 85 in our gene list) of the genes that were positively regulated are *alg-3/4* 5′–targeted genes, while three-fourths (25 of 34 in our gene list) of the negatively regulated genes are *alg-3/4* 3′–targeted genes. This observation is in line with the current knowledge of spermiogenesis-associated piRNAs in mammals, which regulate their targeted genes posttranscriptionally (*4*).

DISCUSSION

Model of *alg-3/4* 26G small RNA generation and cellular effects

ERI/DICER is the core protein complex involved in *alg-3/4* 26G small RNA biogenesis, and previous studies have identified more than 10 proteins in the complex (*7*–*10*, *13*). Here, we show that before initiation of *alg-3/4* 26G small RNA production by the ERI/DICER complex, NYN-3 expresses specifically during spermatogenesis and positioned at 16 to 30% of 5′ end of mature mRNAs. The mRNAs, with a stem-loop structure and an AG-rich motif, cleaved by NYN-3 serve as RNA template for the ERI/DICER complex to initiate *alg-3/4* 26G small RNAs production via RRF-3. During the synthesis of 26G small RNAs, Dicer cleaves the RNA duplex, leaving a 2-nt overhang of sense RNA that can be further used as a template for RRF-3. This action is thought to result in the 2-nt overlapping pattern that is observed with adjacent 26G small RNAs (*6*). ALG-3, and likely ALG-4, is then recruited to a site nearby the ERI/DICER complex, where it is loaded with newly synthesized *alg-3/4* 26G small RNAs and corresponding templates (Fig. 7).

Our data mining of enriched *alg-3/4* 5′– and *alg-3/4* 3′–targeted genes and their association with positively and negatively regulated *alg-3/4* 26G small RNA–targeted genes suggested that genes related to signaling pathways are associated with *alg-3/4* 26G small RNA targeted to the 5′ end of genes and their proteins are mostly positively regulated by 26G small RNAs, while genes targeted by *alg-3/4* 26G RNAs at the 3′ portion related to chromosome organization are mostly negatively regulated by 26G small RNAs. This intriguing correlation warrants further study.

NYN-3 recognizes *alg-3/4*–targeted transcripts via an undetermined mechanism

We performed motif and secondary structure searches for NYN-3 binding regions on *alg-3/4*–targeted transcripts. In doing so, we identified an AG-rich motif and a stem-loop structure. However, the AG-rich motif is neither present in all *alg-3/4*–targeted transcripts nor it is absent in non–*alg-3/4*–targeted transcripts, suggesting that although AG-rich motif is a preferable sequence, it is unlikely the main determinant for NYN-3 recognition. Furthermore, stem-loop structures are present in most RNA sequences, and the structures may be too variable among all *alg-3/4*–targeted sequences for the program to predict. Thus, it is also unlikely that the stem-loop structure alone is responsible for NYN-3 recognition.

Studies on the mouse ZC3h12a gene, *Regnase-1*, have suggested that targeted RNA cleavage via Regnase-1 only takes place in actively translated RNAs via an interaction with UPF1 (up frameshift) (*21*). Thus, it is reasonable to speculate that there are unidentified proteins that guide NYN-3 to specifically cleave the *alg-3/4*–targeted transcripts during spermatogenesis. Our analysis of the 5′ positions of ALG-3–bound capped or triphosphorylated sense RNAs (i.e., the likely RNA template for 26G small RNA biogenesis) suggested that the TSSs of templating transcripts are different from the mRNA

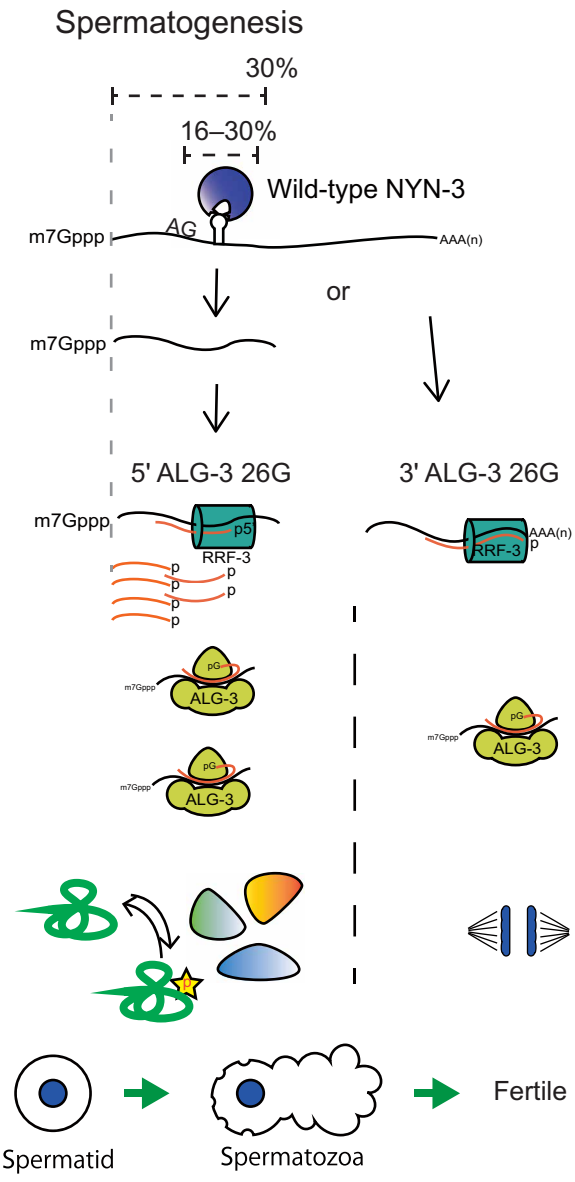

Fig. 7. Model of NYN-3 function in *alg-3/4* 26G small RNA biogenesis and the roles of different *alg-3/4* 26G small RNA subtypes.

capping site identified in hermaphordites/oogenesis, and these alternative TSSs are likely present during male/spermatogenesis. Moreover, a significant motif was found between the alternative TSSs and its corresponding 26G small RNAs. Thus, spermatogenesis-specific protein(s) that specifically associate with mRNA upstream of 26G small RNAs are likely to be candidate proteins that aid NYN-3 found in *alg-3/4*–targeted mRNAs.

Relative position between ePAR-CLIP reads and ALG-3–bound 26G small RNAs

In our ePAR-CLIP-seq experiments, we used the 5′ position of the most abundant ALG-3–bound 26G small RNAs as a reference to identify the relative positions of HA::NYN-3(ht044)–associated RNAs. Because of the phased cycle of 26G small RNAs synthesis, our use of the 5′ end of downstream 26G small RNA (not most abundant) as reference identified RNA fragments in cleaved by HA::NYN-3. Thus, we reanalyze the coverage of ePAR-CLIP reads using 5′ end of downstream 26G small RNA as reference, and, as expected, the ePAR-CLIP-seq identified RNA fragments other than downstream of the 5′ end of 26G small RNA, the reads covered most of the region corresponding to 26G small RNA–targeted sites (fig. S3B). We cannot exclude the possibility that biosynthesis of upstream 26G small RNAs is independent of NYN-3–mediated cleavage. However, the notion that NYN-3–mediated cleavage creates RNA templates for 26G small RNA synthesis is still supported by our findings. For instance, NYN-3 cleavage sites could be identified by 3′ RACE when comparing HA::NYN-3– and HA::NYN-3(ht044)–IPed RNA. Moreover, the decreased abundance of global cap/triphosphorylated RNA templates in ALG-3–bound sense RNAs in *ha::nyn-3(ht044)* and *rrf-3(pk1426)* relative to WT also supports the model that HA::NYN-3 cleaves RNA to create RRF-3 RNA templates.

Potential defects in the *ha:nyn-3(tm2499)* strain

Among all the NYN-3 mutations examined that are used in this study, the precise role of the 68 amino acids that deleted in *nyn-3(tm2499)* remains undetermined. The steady-state protein quantity of HA::NYN-3(tm2499) is comparable to that of HA::NYN-3, and our HA-IP 3′ RACE data and the intact ribonuclease domain suggested that HA::NYN-3(tm2499) is capable of binding to and cleaving targeted *f59a6.2* transcripts. However, the level of ALG-3–bound 26G small RNA is identical to a hypomorph mutant, *ha::nyn-3(ht056)*, suggesting that the 68–amino acid deletion in *ha::nyn-3(tm2499)* makes the protein function as only 20% of protein left. One hypothesis is that the 68 deleted amino acids in *nyn-3* may be involved in cross-talking with RRF-3; therefore, although the targeted mRNAs are properly cleaved, they were not received by the RRF-3 complex as if not sufficient to the targeted mRNAs recognized by *nyn-3* hypomorphic mutant, *ha::nyn-3(ht056)*. However, more experiments are needed to validate this hypothesis.

Untemplated regions are not identified after NYN-3 cleavage

Since the other two RdRPs in *C. elegans*, EGO-1 and RRF-1, are known to recognize untemplated (UG)n sequence on the RNA template, we also performed a search for untemplated regions on the RNA cleaved by NYN-3. However, only 2% of the sequence from the HA::NYN-3 IP *f59a6.2* 3′ RACE was determined to be untemplated sequences of 3 to 5 nt. Furthermore, the percentage of sequences containing untemplated regions was even higher (3.2%) in the HA-IP *f59a6.2* 3′ RACE than in *ha::nyn-3(ht044)*, the cleavage-defective mutant, suggesting that the untemplated regions are not likely to take place after NYN-3 cleavage (fig. S4F).

Differences in the small RNA profiles of total monophosphorylated and ALG-3–bound monophosphorylated small RNA libraries

Although the monophosphorylated antisense small RNAs from male worms were previously shown to largely consist of *alg-3/4* 26G small RNAs, our distribution analysis of mono antisense small RNAs showed that the amounts of small RNAs are comparable between 5′ and 3′ end of genes. In contrast, the mono antisense small RNAs from the ALG-3 IP were preferentially derived from the 5′ end of genes. Since two Argonautes are known to be required for stabilizing *alg-3/4* 26G small RNAs, one possible explanation is that despite

their 96% identity, ALG-3 and ALG-4 might have distinctive functions in regulating *alg-3/4* 26G small RNA–targeted genes. This hypothesis is consistent with the findings of Conine *et al*., (*1*) who showed that the *alg-3(tm1156)* single mutation is sufficient to cause a decreased brood size at 20°and 25°C but it is not sufficient to cause sterility at 25°C; a similar trend was observed with *alg-4(ok1041)*. The *alg-3(tm1156); alg-4(ok1041)* double mutant is sufficient to cause sterility at 25°C, a result that suggests overlapping and distinct functions of ALG-3 and ALG-4. Thus, whether the 26G small RNAs targeting 3′ end of genes are associated with ALG-4 or other Argonautes remains to be examined.

MATERIALS AND METHODS

Genetics

C. elegans culture and genetics were performed as described elsewhere (*28*, *29*). Unless otherwise noted, the WT strain used in this study was the Bristol N2 strain. Alleles used in this study are LG II: *rrf-3(pk1426)*, *ha::nyn-3*, *ha::nyn-3(ht044)*, *ha::nyn-3(tm2499)*, *ha::nyn-3(ht056)*, and *nyn-3(ht075)*; LG IV: *2xflag::alg-3* and *eri-1(mg366)*; and LG V: *fog-2 (q71)*. All affinity tags and point mutations were constructed using CRISPR. The *nyn-3(tm2499)* strain was obtained from the laboratory of S. Mitani, Department of Physiology, Tokyo Women's Medical University School of Medicine, Tokyo, Japan.

In vitro spermatid activation assay

Spermatids were released into 5 μl of 1× sperm salt medium [50 mM Pipes (pH 7.0), 25 mM KCl, 45 mM NaCl, 1 mM $MgSO_4$, and 2 mM $CaCl_2$] containing pronase E (500 μg/ml) (*30*, *31*) on a slide and incubated for 5 min at room temperature before imaging on a ZEISS Axio Imager 2 microscopy system with a 100× objective.

Fluorescence imaging

MSP staining of spermatids

The gonad and spermatids were released in 1× sperm salt medium [50 mM Pipes (pH 7.0), 25 mM KCl, 45 mM NaCl, 1 mM $MgSO_4$, and 2 mM $CaCl_2$] (*30*, *31*). After freeze-cracking, samples were fixed in methanol and acetone for 10 min. The primary anti-MSP (4A5 Hybridoma Bank, Iowa, USA) antibody was applied at a 1:5 dilution, followed by 1:200 dilution of Alexa Fluor 488–conjugated anti-mouse antibody. A ZEISS Axio Imager 2 microscope system with a 100× objective was used to obtain images.

Immunostaining of male gonads

Adult male gonads of *2xflag::alg-3; ha::nyn-3* and tagged mutants were released by decapitating worms on a slide. Extruded gonads were fixed with formaldehyde, followed by permeabilization with freeze-cracking, and staining using 1:50 dilutions of rabbit anti-HA (Cell Signaling Technology, 3724S) and mouse anti-FLAG (Sigma-Aldrich, F1804), according to protocols described previously (*32*). Confocal images were acquired using a Zeiss LSM700 confocal microscope.

RNA immunoprecipitation

The 4-thio-U–based cross-linking method was applied in both ePAR-CLIP and 3′ RACE studies. One millimolar 4-thio-U (Cayman Chemical, Ann Arbor, USA) was mixed in concentrated OP50 (an *Escherichia coli* strain) and fed to L4 adults. After growth at 25°C overnight, HA-tagged WT and *nyn-3* mutants with *2xflag::alg-3* were harvested as gravid adults, and the males were enriched by filtering through a 35-μm mesh (Spectrum Labs, New Brunswick, USA). The male-enriched population was irradiated with 365-nm UV light at 2 J/cm^2 (*33*). After the irradiation, the male-enriched worm pellet was mixed with one volume of homogenization buffer [25 mM Hepes-KOH (pH 7.5), 10 mM potassium acetate, 2 mM magnesium chloride, 0.1% (v/v) NP-40, 110 mM potassium chloride, and SUPERaseIn (200 U/ml) (Ambion)] for all the IP samples; iCLIP lysis buffer (*19*) was used to prepare ePAR-CLIP samples. Eighty microliters (for ePAR-CLIP) or 40 μl (for HA-NYN-3 IP) of anti-HA antibody–conjugated beads (Sigma-Aldrich, St. Louis, USA) per 10 mg of total lysate was applied to the samples and incubated at 4°C for 16 hours. Alternatively, 20 μl of anti-FLAG antibody–conjugated beads (Sigma-Aldrich) was used per 10 mg of total lysate for 2xFLAG::ALG-3 IP; the samples were incubated with beads for 1 hour at 4°C. The wash procedures for ePAR-CLIP were according to the original protocol (*19*), while three washes with 1 ml of homogenization buffer were performed for the other IPs. For 4-thio-U–cross-linked RNA, 100 μl of proteinase K (0.5 mg/ml), 10 mM EDTA, 100 mM tris-HCl (pH 7.4), 50 mM NaCl, and SUPERaseIn (200 U/ml) were incubated at 37°C for 20 min to digest proteins. Then, total RNA from IP samples was extracted with TRIzol reagent (Ambion) following the manufacturer's protocol. For targeted RNA quantification, the extracted RNA was subjected to reverse transcription using SuperScript IV (Life Technologies) and a mixture of random hexamers and *f59a6.2* reverse primers. Quantitative PCR was used to measure the level of *f59a6.2* mRNA IPed by HA::NYN-3(ht044). The level was normalized to *act-3*. The sequences of oligonucleotides used for the RT-qPCR experiments are listed in table S3.

Small RNA cloning

NucleoZOL (Machery-Nagel, Allentown, USA)–extracted total RNA, the small RNA-enriched fraction, and TRIzol-extracted 2XFLAG::ALG-3-associated RNAs were subjected to 15% (w/v) acrylamide/7M urea denaturing gel electrophoresis with tris-borate EDTA (TBE) as the running buffer. RNAs ranging in size between 18 and 60 nt were gel-purified and cloned, either with or without treatment of RppH [New England Biolabs (NEB), Ipswich, USA]. The rest of the cloning procedures was performed as described previously (*1*, *16*, *34*), except the cloning primers that were adjusted for the Illumina platform (table S3).

3′ RACE

RNA extracted from HA-IPs was ligated to DNA oligos at the 3′ end, with the 3′ consensus region of Illumina P5 sequence, which was preactivated with *Mth* RNA Ligase (NEB). For the 3′ RACE analyzed on 22% 1× TBE-PAGE, the same preactivated 3′ ligation primer for small RNA cloning was used for smaller size PCR amplicons to improve resolution on the PAGE. The ligation procedure followed the non–adenosine triphosphate ligation step in small RNA cloning (*16*). Ligation products were reverse-transcribed using a primer complementary to the ligated sequence. The nested PCR procedure was used to specifically amplify the cleavage products; cDNAs were amplified (20 cycles) using the first-strand cDNA primer and a forward gene–specific primer that targeted a site slightly beyond 26G small RNA corresponding sequence. Amplicons of 50 to 100 bp (including at least 50 nt downstream of each 26G small RNA initiation site in the mRNA) were size-selected on a native 8% (w/v) polyacrylamide gel. For samples analyzed on 22% native PAGE, the cycle number for the final PCR was first determined by qPCR, and the

amplified amplicons were analyzed on 22% 1× TBE-PAGE run at 4 mA and 100 V for 16 hours. SYBR Green II RNA gel stain (Thermo Fisher Scientific) was used to visualize the PCR amplicons. Since long adaptor sequences can be recognized and used in the Illumina machine, two consecutive PCRs were performed. First, a region between the 26G small RNA corresponding sequences and ligated sequence was amplified. Second, a PCR was performed to incorporate barcodes and the rest of the P5 and P7 sequences. The cycle number was first determined using previously described cycle estimation procedures (*19*). The 3′ RACE products were then amplified according to the estimated Ct value, with the last 6 cycles using a specific barcode with full-length Illumina sequence added to each sample. The final amplicons (140 to 300 bp) were excised, eluted, and used as the input for Illumina sequencing.

Illumina sequencing and data analysis

The DNAs subject to sequencing were all quantified by Qbit and pooled into one single lane. The pooled DNAs were then run on an Illumina HiSeq 2500 at the High-Throughput Genomics Core at BRCAS (Biodiversity Research Center in Academia Sinica), Academia Sinica, Taipei, Taiwan.

Data analysis on small RNA-seq and ePAR-CLIP-seq

All reads from ePAR-CLIP and small RNA-seq libraries were first trimmed to eliminate the adaptor sequence at the 3′ or 5′ terminus. For small RNA-seq, identical sequences were first summed to obtain counts of each unique sequence. All reference sequences were derived from the most updated version of wormbase (WS281), and alignment was performed with Bowtie 1.3.0 (http://bowtie-bio.sourceforge.net/index.shtml) (*35*). The trimmed ePAR-CLIP reads and rearranged reads for small RNAs were sequentially aligned to the genome and cDNA database. Reads that matched various categories of genes were assigned and summed. For small RNA libraries, normalized reads were defined as rpm total reads matching nonstructural RNAs (nonribosomal RNA nor nontransfer RNA). For the IP samples, normalized reads were defined as rpm (unless otherwise noted) total reads matching the *C. elegans* genome.

3′ RACE-seq analysis

Since our design has the 3′ ligated oligo as part of illumine sequence from P5, thus we first search for primer sequences, which contain part of P7 sequence and 26G small RNA sequence. The sequence between 26G small RNA sequence and the beginning of the reads is the sequence between 26G small RNA and cleavage sites. The length distribution of trimmed sequences was calculated and normalized to their respective total reads. All analyses were performed using custom Python scripts, which can be requested or found at github (https://github.com/ntuimmtsai).

SUPPLEMENTARY MATERIALS

Supplementary material for this article is available at https://science.org/doi/10.1126/sciadv.abm0699

View/request a protocol for this paper from *Bio-protocol*.

REFERENCES AND NOTES

1. C. C. Conine, P. J. Batista, W. Gu, J. M. Claycomb, D. A. Chaves, M. Shirayama, C. C. Mello, Argonautes ALG-3 and ALG-4 are required for spermatogenesis-specific 26G-RNAs and thermotolerant sperm in Caenorhabditis elegans. *Proc. Natl. Acad. Sci. U.S.A.* **107**, 3588–3593 (2010).
2. W. Deng, H. Lin, miwi, a murine homolog of piwi, encodes a cytoplasmic protein essential for spermatogenesis. *Dev. Cell* **2**, 819–830 (2002).
3. T. Han, A. P. Manoharan, T. T. Harkins, P. Bouffard, C. Fitzpatrick, D. S. Chu, D. Thierry-Mieg, J. Thierry-Mieg, J. K. Kim, 26G endo-siRNAs regulate spermatogenic and zygotic gene expression in Caenorhabditis elegans. *Proc. Natl. Acad. Sci. U.S.A.* **106**, 18674–18679 (2009).
4. P. Dai, X. Wang, L.-T. Gou, Z.-T. Li, Z. Wen, Z.-G. Chen, M.-M. Hua, A. Zhong, L. Wang, H. Su, H. Wan, K. Qian, L. Liao, J. Li, B. Tian, D. Li, X.-D. Fu, H.-J. Shi, M.-F. Liu, A translation-activating function of MIWI/piRNA during mouse spermiogenesis. *Cell* **179**, 1566–1581.e16 (2019).
5. C. C. Conine, J. J. Moresco, W. Gu, M. Shirayama, D. Cone Jr., J. R. Yates III, C. C. Mello, Argonautes promote male fertility and provide a paternal memory of germline gene expression in C. elegans. *Cell* **155**, 1532–1544 (2013).
6. D. A. Chaves, H. Dai, L. Li, J. J. Moresco, M. E. Oh, D. Conte Jr., J. R. Yates III, C. C. Mello, W. Gu, The RNA phosphatase PIR-1 regulates endogenous small RNA pathways in C. elegans. *Mol. Cell* **81**, 546–557.e5 (2021).
7. M. V. Almeida, S. Dietz, S. Redl, E. Karaulanov, A. Hildebrandt, C. Renz, H. D. Ulrich, J. König, F. Butter, R. F. Ketting, GTSF-1 is required for formation of a functional RNA-dependent RNA polymerase complex in *Caenorhabditis elegans*. *EMBO J.* **37**, e99325 (2018).
8. C. Thivierge, N. Makil, M. Flamand, J. J. Vasale, C. C. Mello, J. Wohlschlegel, D. Conte Jr., T. F. Duchaine, Tudor domain ERI-5 tethers an RNA-dependent RNA polymerase to DCR-1 to potentiate endo-RNAi. *Nat. Struct. Mol. Biol.* **19**, 90–97 (2011).
9. D. M. Pavelec, J. Lachowiec, T. F. Duchaine, H. E. Smith, S. Kennedy, Requirement for the ERI/DICER complex in endogenous RNA interference and sperm development in Caenorhabditis elegans. *Genetics* **183**, 1283–1295 (2009).
10. J. I. Gent, M. Schvarzstein, A. M. Villeneuve, S. G. Gu, V. Jantsch, A. Z. Fire, A. Baudrimont, A Caenorhabditis elegans RNA-directed RNA polymerase in sperm development and endogenous RNA interference. *Genetics* **183**, 1297–1314 (2009).
11. T. F. Duchaine, J. A. Wohlschlegel, S. Kennedy, Y. Bei, D. Conte Jr., K. Pang, D. R. Brownell, S. Harding, S. Mitani, G. Ruvkun, J. R. Yates III, C. C. Mello, Functional proteomics reveals the biochemical niche of C. elegans DCR-1 in multiple small-RNA-mediated pathways. *Cell* **124**, 343–354 (2006).
12. A. Shukla, J. Yan, D. J. Pagano, A. E. Dodson, Y. Fei, J. Gorham, J. G. Seidman, M. Wickens, S. Kennedy, Poly(UG)-tailed RNAs in genome protection and epigenetic inheritance. *Nature* **582**, 283–288 (2020).
13. H. Y. Tsai, C. C. G. Chen, D. Conte Jr., J. J. Moresco, D. A. Chaves, S. Mitani, J. R. Yates III, M. D. Tsai, C. C. Mello, A ribonuclease coordinates siRNA amplification and mRNA cleavage during RNAi. *Cell* **160**, 407–419 (2015).
14. K. Matsushita, O. Takeuchi, D. M. Standley, Y. Kumagai, T. Kawagoe, T. Miyake, T. Satoh, H. Kato, T. Tsujimura, H. Nakamura, S. Akira, Zc3h12a is an RNase essential for controlling immune responses by regulating mRNA decay. *Nature* **458**, 1185–1190 (2009).
15. M. A. Miller, V. Q. Nguyen, M. H. Lee, M. Kosinski, T. Schedl, R. M. Caprioli, D. Greenstein, A sperm cytoskeletal protein that signals oocyte meiotic maturation and ovulation. *Science* **291**, 2144–2147 (2001).
16. W. Gu, M. Shirayama, D. Conte Jr., J. Vasale, P. J. Batista, J. M. Claycomb, J. J. Moresco, E. M. Youngman, J. Keys, M. J. Stoltz, C.-C. G. Chen, D. A. Chaves, S. Duan, K. D. Kasschau, N. Fahlgren, J. R. Yates III, S. Mitani, J. C. Carrington, C. C. Mello, Distinct argonaute-mediated 22G-RNA pathways direct genome surveillance in the C. elegans germline. *Mol. Cell* **36**, 231–244 (2009).
17. J. M. Claycomb, P. J. Batista, K. M. Pang, W. Gu, J. J. Vasale, J. C. van Wolfswinkel, D. A. Chaves, M. Shirayama, S. Mitani, R. F. Ketting, D. Conte Jr., C. C. Mello, The Argonaute CSR-1 and its 22G-RNA cofactors are required for holocentric chromosome segregation. *Cell* **139**, 123–134 (2009).
18. M. Hafner, M. Landthaler, L. Burger, M. Khorshid, J. Hausser, P. Berninger, A. Rothballer, M. Ascano Jr., A. C. Jungkamp, M. Munschauer, A. Ulrich, G. S. Wardle, S. Dewell, M. Zavolan, T. Tuschl, Transcriptome-wide identification of RNA-binding protein and microRNA target sites by PAR-CLIP. *Cell* **141**, 129–141 (2010).
19. E. L. Van Nostrand, G. A. Pratt, A. A. Shishkin, C. G.-Burkhart, M. Y. Fang, B. Sundararaman, S. M. Blue, T. B. Nguyen, C. Surka, K. Elkins, R. Stanton, F. Rigo, M. Guttman, G. W. Yeo, Robust transcriptome-wide discovery of RNA-binding protein binding sites with enhanced CLIP (eCLIP). *Nat. Methods* **13**, 508–514 (2016).
20. V. Anantharaman, L. Aravind, The NYN domains: Novel predicted RNAses with a PIN domain-like fold. *RNA Biol.* **3**, 18–27 (2006).
21. T. Mino, Y. Murakawa, A. Fukao, A. Vandenbon, H. H. Wessels, D. Ori, T. Uehata, S. Tartey, S. Akira, Y. Suzuki, C. G. Vinuesa, U. Ohler, D. M. Standley, M. Landthaler, T. Fujiwara, O. Takeuchi, Regnase-1 and roquin regulate a common element in inflammatory mRNAs by spatiotemporally distinct mechanisms. *Cell* **161**, 1058–1073 (2015).
22. H. I. Suzuki, M. Arase, H. Matsuyama, Y. L. Choi, T. Ueno, H. Mano, K. Sugimoto, K. Miyazono, MCPIP1 ribonuclease antagonizes dicer and terminates microRNA biogenesis through precursor microRNA degradation. *Mol. Cell* **44**, 424–436 (2011).

23. R. Lorenz, S. H. Bernhart, C. H. Z. Siederdissen, H. Tafer, C. Flamm, P. F. Stadler, I. L. Hofacker, ViennaRNA Package 2.0. *Algorithms Mol. Biol.* **6**, 26 (2011).
24. A. R. Gruber, R. Lorenz, S. H. Bernhart, R. Neubock, I. L. Hofacker, The Vienna RNA websuite. *Nucleic Acids Res.* **36**, W70–W74 (2008).
25. W. Gu, H.-C. Lee, D. Chaves, E. M. Youngman, G. J. Pazour, D. Conte Jr., C. C. Mello, CapSeq and CIP-TAP identify Pol II start sites and reveal capped small RNAs as C. elegans piRNA precursors. *Cell* **151**, 1488–1500 (2012).
26. P. Kueng, Z. Nikolova, V. Djonov, A. Hemphill, V. Rohrbach, D. Boehlen, G. Zuercher, A. C. Andres, A. Ziemiecki, A novel family of serine/threonine kinases participating in spermiogenesis. *J. Cell Biol.* **139**, 1851–1859 (1997).
27. C. H. Wong, C. Y. Cheng, Mitogen-activated protein kinases, adherens junction dynamics, and spermatogenesis: A review of recent data. *Dev. Biol.* **286**, 1–15 (2005).
28. S. Brenner, The genetics of Caenorhabditis elegans. *Genetics* **77**, 71–94 (1974).
29. A. K. Corsi, B. Wightman, M. Chalfie, A transparent window into biology: A primer on Caenorhabditis elegans. *WormBook* , 1–31 (2015).
30. D. C. Shakes, S. Ward, Initiation of spermiogenesis in C. elegans: A pharmacological and genetic analysis. *Dev. Biol.* **134**, 189–200 (1989).
31. G. A. Nelson, S. Ward, Vesicle fusion, pseudopod extension and amoeboid motility are induced in nematode spermatids by the ionophore monensin. *Cell* **19**, 457–464 (1980).
32. C. M. Phillips, K. L. McDonald, A. F. Dernburg, Cytological analysis of meiosis in Caenorhabditis elegans. *Methods Mol. Biol.* **558**, 171–195 (2009).
33. A. C. Jungkamp, M. Stoeckius, D. Mecenas, D. Grün, G. Mastrobuoni, S. Kempa, N. Rajewsky, In vivo and transcriptome-wide identification of RNA binding protein target sites. *Mol. Cell* **44**, 828–840 (2011).
34. J. J. Vasale, W. Gu, C. Thivierge, P. J. Batista, J. M. Claycomb, E. M. Youngman, T. F. Duchaine, C. C. Mello, D. Conte Jr., Sequential rounds of RNA-dependent RNA transcription drive endogenous small-RNA biogenesis in the ERGO-1/Argonaute pathway. *Proc. Natl. Acad. Sci. U.S.A.* **107**, 3582–3587 (2010).
35. B. Langmead, C. Trapnell, M. Pop, S. L. Salzberg, Ultrafast and memory-efficient alignment of short DNA sequences to the human genome. *Genome Biol.* **10**, R25 (2009).

Acknowledgments: We thank V. Gopalan, Ohio State University, Columbus, OH, USA, for comments on the manuscript. *Nyn-3(tm2499)* was provided by S. Mitani, Tokyo Women's Medical University, School of Medicine, Tokyo, Japan, and C. Mello, University of Massachusetts Medical School, Worcester, MA, USA. *Rrf-3(pk1426)* and *eri-1(mg366)* were provided by the Caenorhabditis Genetics Center, which is funded by NIH Office of Research Infrastructure Programs (P40 OD010440). We thank The C. elegans Core Facility of the National Core Facility for Biopharmaceuticals, Ministry of Science and Technology, Taiwan, for helping with various worm-related equipment and reagents. We also thank NGS High Throughput Genomics Core at the Biodiversity Research Center, Academia Sinica for all the Illumina sequencing. The latest database and gene enrichment tools can be found in WormBase. **Funding:** This study was funded by grants from the Ministry of Science and Technology (MOST) of Taiwan (105-2320-B-002-006-MY3, 105-2320-B-002-061-MY3, 107-3017-F-002-002, 108-2320-B-002-075-MY3, and 110-2634-F-002-044), the Ministry of Education in Taiwan, National Taiwan University (110L901402B), and National Taiwan University (108 L7854, 109 L7854, 110 L7804, and 110 L893404). **Author contributions:** Experimental design, obtaining CRISPR lines, all RNA-seq–related experiments, data analysis, and manuscript writing were done by H.-Y.T. Brood size counting, in vitro spermatids activation, and HA tagging *nyn-3(tm2499)* and *nyn-3(tm2499)* rescue lines were done by H.-T.C. Brood size counting for *nyn-3(ht056)* and *nyn-3(ht075)* and manual sequencing from HA-IP 3′ RACE were done by Y.-T.T. **Competing interests:** The authors declare that they have no competing interests. **Data and materials availability:** All data needed to evaluate the conclusions in the paper are present in the paper and/or the Supplementary Materials. The raw data and scripts are also available from DRYAD (doi:10.5061/dryad.b8gtht7ft) and GEO under the accession number PRJNA756853. All newly generated *C. elegans* strains are available upon request.

Submitted 29 August 2021
Accepted 27 June 2022
Published 10 August 2022
10.1126/sciadv.abm0699